Freie Universität Berlin

A Tensor Network Study of the Spin-1/2 Heisenberg Antiferromagnet on the Floret Pentagonal Lattice

Master Thesis

Author: Finn Martin Krein
Supervisor: Prof. Dr. Jens Eisert
Advisors: Jan Naumann & Dr. Philipp Schmoll

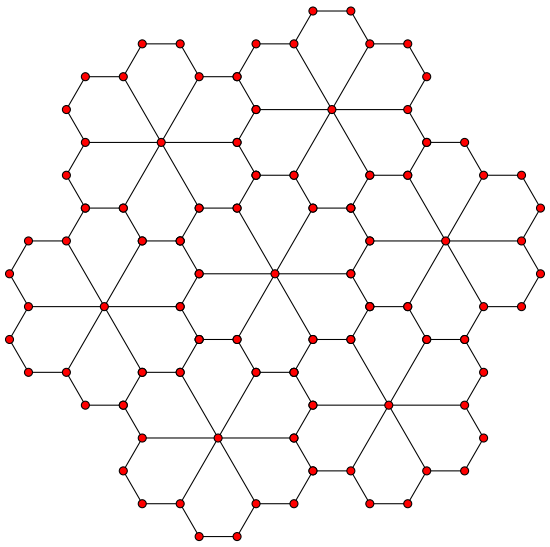

March 15, 2024

Acknowledgements

I would like to express my sincere gratitude to my supervisors Jan Naumann and Philipp Schmoll, for their patience, guidance and for teaching me so much in the process of this thesis.

Additionally, I would like to give thanks to Jens Eisert and the AG-Eisert for fostering a vibrant and stimulating environment. Their diverse perspectives and lively discussions have broadened my horizons and enriched my learning experience.

Also I want to thank the Freie Universität Berlin and the IT support of the physics department for providing bespoke computing hardware with the Curta [1] and Sheldon clusters, without which the numerical simulations of this thesis would have been impossible.

Finally, I would like to thank Alex Penner for helpful insights and discussions, as well as Arvid and Jule for patiently listening to me talk about my thesis.

Contents

1 Introduction

Entanglement is at the heart of what distinguishes quantum phenomena from the world of classical physics. Although quantum phenomena primarily occur at small length scales, the collective behaviour of entangled quantum many-body states can give rise to macroscopic quantum effects. An area demonstrating these macroscopic consequences of quantum effects is quantum magnetism, where spin lattices exhibit emergent behavior governed by complex entanglement patterns between the particles.

In the area of quantum many-body physics and magnetism, the topic of frustrated magnetism shows particularly rich and interesting behavior, such as spontaneous breaking of lattice symmetries and magnetization plateaus. Investigation of frustrated quantum magnets discovered exotic phases, such as spin ice and quantum spin liquids.

Spin ice, a phase first reported for pyrochlore $Ho_2Ti_2O_7$ crystals [2], is suspect to a geometric frustration similar to that of water ice, resulting in extensive residual entropy at zero temperature. The spin ice phase famously hosts excitations that are magnetic monopoles [3].

Another prominent phase related to frustrated quantum magnetism is the quantum spin liquid. Quantum spin liquids (QSL) were proposed by Anderson [4] as paramagnetic states bearing no magnetic long-range order without spontaneous breaking of lattice symmetry. Strikingly, quantum spin liquids are capable of fractional excitations known as spinons, charge neutral quasiparticles with spin $S = \frac{1}{2}$. Understanding quantum spin liquids bears relevance for technical applications, as they have been suggested as possible explanation for high temperature superconductors [5] and show topological order [6], which could find application in fault tolerant quantum computing.

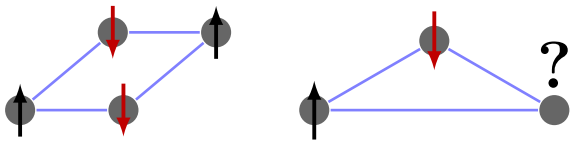

Figure 1.1: Antiferromagnetic spins in a square (left) and in a triangle (right).

These complex phenomena were encountered in the study of geometrically frustrated antiferromagnets, lattices in which spins want to align against each other to minimize their exchange energy. The dilemma of frustration is most easily illustrated by three spins arranged in a triangle. If two of the spins align against each other there is no

way for the third spin to align against both its neighbors (see Fig. 1.1). Classically, the energetically optimal configuration will consist of a "compromise". This demonstrates a general property of frustration: The global energetically optimal configuration does not satisfy each individual contribution to the energy. As a consequence of frustration the classical ground state of such systems is typically macroscopically degenerate, leading to strong fluctuations at just small temperatures. In frustrated quantum magnets this ground state degeneracy can be lifted by quantum fluctuations, an effect known as order-by-disorder [7].

Studying quantum many-body systems such as quantum magnets numerically faces a grave problem: The Hilbert space of a general quantum state grows exponentially with system size. But many-body states are governed by physical laws which typically feature local interactions, in turn leading to mostly local entanglement structures. Ground states of 1D gapped Hamiltonians are restricted by an area law [8], limiting the growth of entanglement entropy of a region and its complement to their bounding area.

Tensor networks are a class of approaches operating on this paradigm of bounded entanglement, constructing quantum states from many correlated building blocks, each representing a part of the quantum degrees of freedom.

The origin of these methods are found in the study of one dimensional quantum systems. Matrix product states (MPS) [9] represent quantum states as a chain of tensors and are equipped with the density matrix renormalization group (DMRG) [10], a powerful variational technique to obtain the ground state in terms of an MPS. Projected entangled pair states (PEPS) [11] are a generalization of the MPS approach to higher dimensions and have been particularly successful in studying two dimensional systems. To study solid state materials in the thermodynamic limit an infinite variant of PEPS (iPEPS) [12] can be used, representing the lattice by a repeating unit cell of tensors.

Research in frustrated antiferromagnetic materials has historically focused on lattices consisting of triangular units of frustration, such as the triangular lattice [13, 14, 15] or the Kagomé lattice [16, 17, 18, 19]. While examinations of these lattices proved fruitful and many existing frustrated materials are related to these lattices, the study of lattices with larger units of frustration could provide further insight into what constitutes the special properties of frustrated magnetism.

To this end, this thesis aims to investigate frustrated magnetism in pentagonal lattices at the example of the Heisenberg antiferromagnet on the floret pentagonal lattice. This model has previously been studied using exact diagonalization of finite sized clusters [20, 21]. Using lattice periodic tensor network methods we aim to provide another perspective on this problem, focusing on the behaviour of the system in the thermodynamic limit.

In Chapter 2, we will give an introduction to the tensor network methods used to study the model. We start out by discussing the problem of simulating quantum states on a classical computer and how tensor networks approach to solve this problem. Next, we describe the basic principles of tensor networks and present the most relevant tensor network representations of quantum states in one and two dimensions. We then deal with the issue of calculating expectation values on two dimensional tensor network states, focusing on the two methods which were applied in this thesis. After this, we present two different methods of finding the best ground state approximation for a given 2D tensor network ansatz. Finally we discuss a way of calculating correlation lengths in tensor network states.

Chapter 3 consists of our investigation of the Heisenberg model on the floret pentagonal lattice using the introduced tensor network methods. We first introduce the floret pentagonal lattice and define the model Hamiltonian to then briefly discuss the results of previous investigations. We then report our results obtained using simple update imaginary time evolution, and discuss the difficulties in obtaining accurate expectation values on the resulting states. After that we present our simulations using the variational update method and report results for ground state symmetry, ground state energy for the model without external magnetic field as well as results examining the magnetization process of the model.

Finally we give a conclusion of the thesis and an outlook of possible directions for further investigation of frustrated magnetism on the floret pentagonal lattice and other pentagonal lattices.

2 Introduction into Tensor Network Methods

2.1 Why do we need Tensor Networks

As set out in the introduction we want to study frustrated many-body systems on a classical computer, probing important properties like ground state energies and magnetization profiles.

To numerically approach the calculation of interesting physical observables we need to represent the quantum states of our many-body systems on the computer. The Hilbert space $\mathcal{H}$ for a general quantum state with a number of N qubits is growing exponentially with the system size

$$|\psi\rangle \in \mathcal{H} \simeq \mathbb{C}^{2^N}. \tag{2.1}$$

Storing a single complex number in double precision takes 16 bytes, so a state of 9 qubits will take up 9 kilobyte and a state of 36 qubits would take up one terabyte. From this it is apparent that representing and operating on a general quantum state is only feasible up to a certain system size, limited by the capabilities of current computing hardware. Numerically operating on quantum many-body systems as general quantum states is therefore infeasible for even moderate system sizes.

On the other hand the structure of these many body states is determined by the physical laws governing them. For physical systems with local interactions, quantum correlations will often be constrained in some manner (e.g. lattice models), limiting the amount of entanglement of these states. For such states with restricted entanglement structure it might not be necessary to use general quantum states to describe the whole system accurately.

In practice it turns out that there are subsets of the general quantum states that we know how to efficiently represent and compute with classical computers. In particular it is known that in 1D ground states of gapped local Hamiltonians have to obey area laws [8], limiting the growth in entanglement entropy of a region to the bounding area of the region instead of its volume. This is a strong limitation and confines the states satisfying an area law to a small corner of the Hilbert space (see Fig. 2.1).

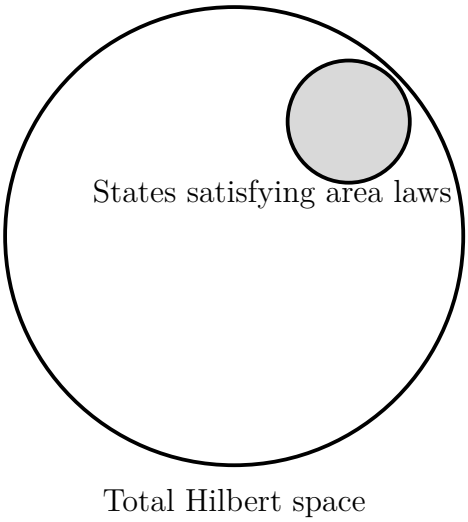

Figure 2.1: Area law states are just a small region of the total Hilbert space.

The states in this subspace exhibit a limited local entanglement that makes them good candidates to try to represent them as tensor network states. Tensor network states represent quantum states by a network of tensor nodes which, when contracted along the network's edges, yield a state in the original Hilbert space. In contrast to a general quantum state the information required to store a tensor network state does not need to scale exponentially with the size of the system. Some quantum states like the resonating valence bond state can be exactly represented by tensor networks with low dimensional tensors [22], while other states can be approximated using tensors of limited dimension, increasing the fidelity of the approximation with the size of the tensors.

While in 1D it has been shown that area-law states can be efficiently represented by tensor networks [8], in higher dimensions an efficient representation can not be found for all states in this sub-region [23]. Regardless, it is expected that for ground states of gapped 2D Hamiltonians the tensor network description is still a valid numerical approach.

For completeness we want to note that there are other methods available to study many-body systems including exact diagonalization [20] and quantum Monte Carlo methods. Methods of the former category are subjected to the exponential scaling detailed above and can therefore only simulate systems of small size and do not reach the thermodynamic limit. Quantum Monte Carlo methods suffer from the sign problem at low temperatures [24].

2.2 Representing Quantum states with Tensor Networks

As outlined above large classes of physically relevant quantum states can be represented or approximate by tensor networks. As there are many different kinds of many body quantum systems there are various ways of modeling these systems with tensor networks. We will focus on the methods most relevant to our problem of studying frustrated quantum magnets in the thermodynamic limit.

At the start of this section we will explain the basic process of splitting a quantum state into multiple parts via the Schmidt decomposition, and introduce some of the most common methods which can be applied to represent many body quantum states in one or two dimensions via tensor networks. We also present a method to represent infinite lattices using tensor networks in order to study quantum states in the thermodynamic limit.

2.2.1 Schmidt Decomposition

A general quantum state of a composite Hilbert space $\mathcal{H} = \mathcal{H}_A \otimes \mathcal{H}_B$ can be written in joined orthogonal basis $\{|\psi_A^i\rangle \otimes |\psi_B^j\rangle\}_{(ij)}$ of the two subspaces with basis $\{|\psi_A^i\rangle\}_i$ and $\{|\psi_B^i\rangle\}_i$

$$|\psi\rangle = \sum_{ij} M_{ij} |\psi_A^i\rangle |\psi_B^j\rangle . \tag{2.2}$$

Here the matrix M_{ij}, with $\dim \mathcal{H}_A \cdot \dim \mathcal{H}_B$ entries encodes the amplitudes of combinations of the different basis vectors. To reduce the dimensionality of this description and separating the descriptions of both systems it would be desirable to express it in terms of an eigendecomposition but M is not necessarily hermitian or square, so such a decomposition of the matrix does not in general exist.

Instead, by diagonalizing $M^\dagger M$ (for matrix M with shape $m \times n$ with $m \geq n$, otherwise $MM^\dagger$) one can obtain the singular value composition (SVD), rewriting M as

$$M = U\Sigma V^\dagger, \tag{2.3}$$

where Σ is a diagonal positive semi-definite real matrix and U and V are (semi-)unitary matrices.

Applying the SVD to the composite state Eq. (2.2) yields

$$\begin{aligned} |\psi\rangle &= \sum_{ij} \sum_{k} U_{ik} \Sigma_k V^\dagger_{kj} \left|\psi^i_A\right\rangle \left|\psi^j_B\right\rangle \\ &= \sum_{k} \Sigma_k \left|\varphi^k_A\right\rangle \left|\varphi^k_B\right\rangle \text{, with} \end{aligned} \tag{2.4}$$

$$\left|\varphi^k_A\right\rangle = \sum_i U_{ik} \left|\psi^i_A\right\rangle \quad \text{and} \quad \left|\varphi^k_B\right\rangle = \sum_j V^\dagger_{kj} \left|\psi^j_B\right\rangle . \tag{2.5}$$

This representation of a general quantum state as a single sum of orthogonal product states is known as the Schmidt decomposition. The Σ_k are known as Schmidt values, the $\left|\varphi^k_A\right\rangle$ and $\left|\varphi^k_B\right\rangle$ are called Schmidt vectors. The Schmidt decomposition is at the heart of constructing tensor network states by enabling the representation of the whole state as a sum (contraction) of amplitude vectors of subspaces which can be independently stored and operated on.

Applying the Schmidt decomposition to a bipartite quantum state yielded a set of vectors representable as a matrix. For a decomposition into multiple parts as for a lattice structure, the Schmidt decomposition can be applied successively, yielding a set of matrices, which can be represented as a tensor of higher rank.

2.2.2 Tensors and Operations on Tensors

Tensors can be described as elements of a tensor product space of vector spaces V and dual spaces V^*. A tensor of contravariant order n and covariant order m is thus

$$T^n_m \in V_1 \otimes ... V_n \otimes V^*_1 \otimes ... \otimes V^*_m. \tag{2.6}$$

For the purposes of modeling quantum states, V_i will usually be $\mathbb{C}^{n_i}$ for some dimension n_i of the individual composite spaces. According to the Riesz representation theorem, complex Hilbert spaces are isometrically isomorphic to their dual spaces, so contravariant dimensions can be converted to covariant ones and vice versa. As tensor product spaces their dimension is the product of the dimensions of the individual spaces

$$\dim(T^n_m) = \left(\prod_{i=1}^{n} \dim(V_i)\right) \left(\prod_{j=1}^{m} \dim(V^*_j)\right). \tag{2.7}$$

For example, a tensor of k D-dimensional vector spaces would have dimension D^k, a dimension scaling exponentially with the number of vector spaces and polynomially with the dimension of the individual spaces.

In numerical practice, tensors are stored as a multidimensional arrays of complex numbers to some basis with an index for each vector and dual space of the respective tensor product space.

The most common operations on tensors in tensor network methods are contractions, reshaping and the above described Schmidt decomposition (or equivalently SVD).

A tensor contraction is a joint summation of two tensors A and B over an index belonging to a vector space on one of the tensors and an index belonging to a dual space on the other tensor

$$C = \sum_i A_i B_i, \tag{2.8}$$

where we omit indices which are not summed over. The dimension of the resulting tensor C is the product of the dimensions of the spaces which were not summed over. Tensors indices can also be contracted with two indices of the same tensor which is referred to as tracing out the indices. Contraction of two tensors can be regarded as tracing over indices of the tensor product of the two tensors.

For numerical methods we are naturally interested in the computational cost of an operation. The numerical cost of tensor contraction over the index i is of the order of

$$\mathcal{O}\left(\dim V_i \prod_j \dim(V_j)\right), \tag{2.9}$$

where the V_j are the vector/dual spaces which are not summed over. When contracting a network of tensors, the contraction order does not change the result, but because the contraction cost depends on the dimensions of the contracted tensors, the total cost of contracting a tensor network in general depends on the order of contractions.

Reshaping a tensor is on one hand the act of converting covariant and contravariant dimensions, for example converting the tensor to a vector/dual vector by combining all dimensions into covariant/contravariant indices. On the other hand it can also refer to grouping multiple indices together into a higher dimensional indices like grouping all covariant and all contravariant indices to turn the tensor into a matrix. Numerically reshaping does not need to change the array storing the data of the tensor.

An tensor can be split into two smaller tensors by reshaping the tensor into a matrix and performing an SVD. This is equivalent to a Schmidt decomposition on the vectorized tensor. Another important application is reducing the dimension of a tensor by truncating the smallest singular values. This is the optimal approximation of the tensor by a lower dimensional tensor, keeping only the most important degrees of correlations of the dimension to the left and right of the SVD. The cost of an SVD is dominated by bidiagonalization and is therefore of the order of $\mathcal{O}(mn^2)$, where m is the larger of the two matrix dimensions and n is the smaller one.

2.2.3 Notation

In the field of tensor network methods, a graphical representation of states and operations is often more comprehensible and easier to write than an algebraic one. The notation customary for tensor networks is known as tensor diagram notation or Penrose graphical notation. We will give a brief introduction to the notation relevant to the discussed tensor network methods.

In tensor diagram notation a (n, m)-tensor is drawn as a box (or other simple shape) with edges protruding from it for each co- and contravariant dimension. The direction an edge is facing often indicates whether it is co- or contravariant, although this convention is not always followed. Shapes without legs represent scalars, while contractions of tensor indices are indicated by joined edges.

Examples of this notation for basic objects, contraction and reshapes can be found in Fig. 2.2.

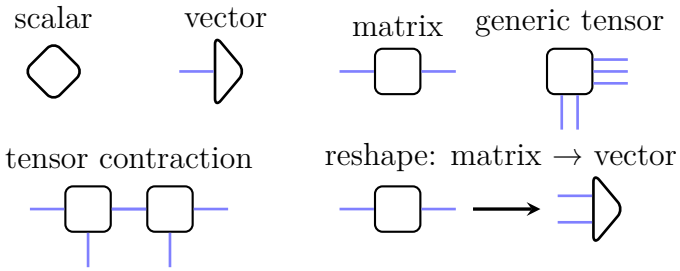

Figure 2.2: Representation of a scalar, a vector, a matrix and a tensor in diagram notation.

2.2.4 Matrix Product States (MPS)

Tensor networks methods aim to split quantum states into multiple tensors which are mutually contracted to mediate physical correlations. A natural and powerful ansatz for one dimensional many-body states are matrix product states (MPS).

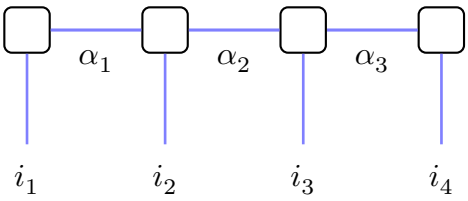

Figure 2.3: Sketch of an MPS with four physical sites and open boundary conditions.

A matrix product state is a tensor network state constructed by serial contraction of tensors (see Fig. 2.3), each of them having an open covariant index (physical index) and two (or one at the edges) contracted indices (bond indices). The dimension of physical indices is referred to as physical dimension p and the maximal dimension of a bond index is the bond dimension χ_B of an MPS.

A general quantum state can be transformed into an MPS by a series of Schmidt decompositions, as illustrated in Fig. 2.4. The parameters $A_j^{i_j}$ of this decomposition

$$|\psi\rangle = \sum_{\{i\}} \prod_{j=0}^{N} A_j^{i_j} |i_1 ... i_N\rangle \tag{2.10}$$

still grow exponentially with system size, the exponential scaling is however transferred to the dimension of the virtual indices of the tensors. The existence of such a transformation shows that MPS with exponentially large bond dimension are able to represent arbitrary quantum states, they are said to be dense.

In order to decrease the states size to enable numerical feasibility on classical computers, we can truncate the lowest singular values following the SVD step. This involves discarding the least significant entanglement correlations for each bond.

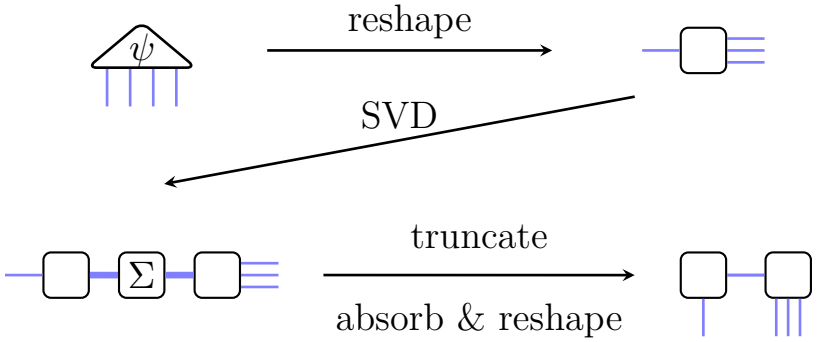

Figure 2.4: Process of transforming a quantum state $|\psi\rangle$ into an MPS.

In Eq. (2.10) for a fixed combination of $\{i_1, ..., i_N\}$ the first $A_0^{i_j}$ and last $A_N^{i_j}$ coefficients will not be matrices but row and column vectors respectively. The chain of contractions has two ends, which is known as an MPS with open boundary conditions. MPS where the first and last tensor are also contracted are called MPS with periodic boundary conditions.

The representation of an MPS is not unique but bears a gauge freedom: Between every pair of closed virtual indices we can insert a matrix and its inverse and absorb it into the neighboring tensors. This leaves the state unchanged but changes the coefficients of the representing tensors.

An especially useful class of gauges are the canonical forms, where the bond indices and tensors coincide with the orthogonal matrices of the Schmidt decomposition across that separation. The example method of consecutive SVDs (Fig. 2.4) will yield a left canonical MPS. In canonical MPS the individual tensors fulfill a notion of orthogonality as illustrated in Fig. 2.5. This properties greatly reduces computational cost for calculating expectation values with canonical MPS.

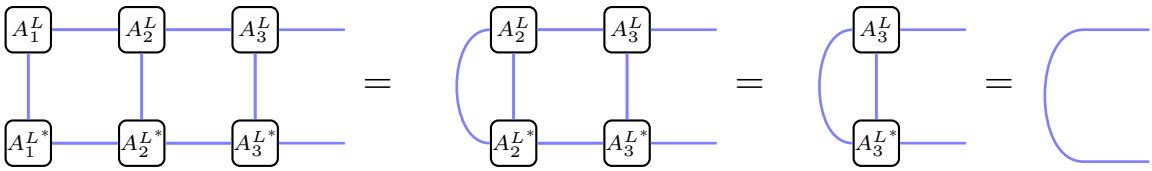

Figure 2.5: Illustration of the orthogonal property of a left canonical MPS.

Contracting the norm of an MPS in canonical form reduces to contracting a single site, e.g. the rightmost for a left canonical state. In contrast, contracting the norm of an MPS for N sites without canonical form, physical dimension p and bond dimension χ_B from left to right costs $\mathcal{O}(Np\chi_\mathrm{B}^3)$ operations.

Instead of converting existing quantum states into MPS, matrix product states are often used as a numerical ansatz to compute ground states of 1D many-body systems. There are various algorithms to optimize the tensor coefficients towards the minimal ground state energy, such as the popular density matrix renormalization group (DMRG) [10] method.

2.2.5 Projected Entangled Pair States (PEPS)

While MPS methods have been successfully employed to study 1D many-body problems, using them to represent two- or three-dimensional systems is not ideal, mainly for two reasons. First, local correlations of 2D systems become long range ones when the states are represented by an MPS. In Fig. 2.6(a) we can see that e.g. a nearest neighbor interaction between sites 1 and 12 have to been mediated by ten MPS sites in between. Applying just a two site operator between these sites would require to contract parts of the tensor network structure back to a general quantum state, defeating the advantages of the tensor network representation.

The second problem is that correlations of MPS decay exponentially [25] with distance in the tensor network. Because in 2D some local correlations would become non-local for an MPS description this would lead to these correlations being exponentially suppressed. As MPS are dense this can be compensated by increasing the bond dimension to grow exponentially with system size, but this would remove the numerical advantages of a tensor network representation.

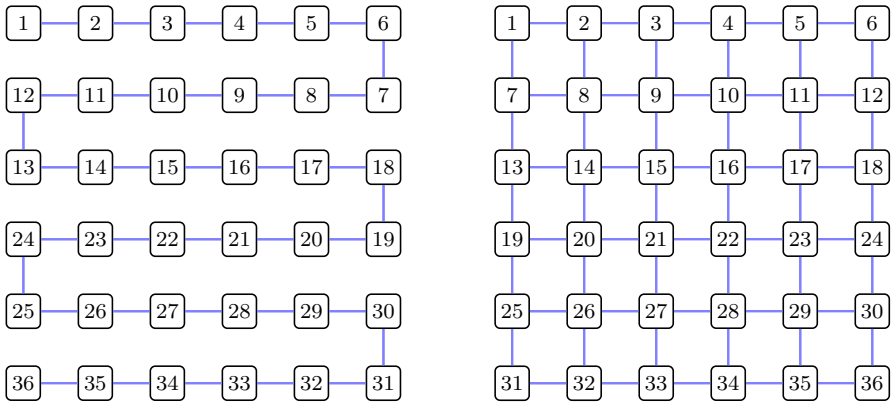

Figure 2.6: (a) An MPS mapped onto a two dimensional lattice. (b) A PEPS state representing a 2D lattice.

A more suitable approach to represent higher dimensional lattices are projected entangled pair states [11] (PEPS), tensor network states consisting of site tensors with an arbitrary amount of neighbors. An example of representing the same square lattice with a PEPS can be found in Fig. 2.6(b). The name PEPS stems from viewing the tensors as projectors connected by jointly projecting maximally entangled pairs. PEPS can be seen as a generalization of MPS to arbitrary physical dimensions. As such, some properties of MPS are also found in PEPS. PEPS fulfill an area law by construction [8] and as MPS have a gauge freedom in every contracted index. As a generalization of MPS, PEPS are also dense.

Still there are also differences between MPS and the more general PEPS [26]:

- *No canonical forms*
  Constructing canonical forms relies on the ability to separate a state into exactly two parts with a Schmidt decomposition. However, for any tensor network state which includes loops this partition is no longer possible. PEPS with $D \geq 2$ always include loops and thus can not be brought into a canonical form. Nevertheless PEPS have a gauge freedom that can be utilized and there have been approaches to introduce quasi-canonical forms for PEPS, retaining some of the orthogonal properties [27, 28].

- *Contraction is hard*
  For PEPS in higher dimensions both exact contraction and finding the optimal contraction order are $\sharp P$-complete [29]. Because exact contraction is so unfeasibly computationally expensive, there exist a number of methods to approximately calculate expectation values of PEPS states. That these approximations work can be justified by the fact that even though general PEPS contraction is $\sharp P$-complete, the approximate calculation of local observables for PEPS states

representing ground states of local gapped Hamiltonians can be achieved in quasi-polynomial time [30].

- *PEPS can represent polynomially decaying correlations*
  In contrast to MPS higher dimensional PEPS can exhibit polynomially decaying correlations [31] and are thus better suited to handle critical states.

2.2.6 Infinite PEPS (iPEPS)

To understand the physics of many-body Hamiltonians it is important to learn about the behavior of the system in the thermodynamic limit. While exact diagonalization is feasible for smaller systems, they suffer from finite size effects and might not accurately describe the properties of the bulk material. The eigenstates of solid state systems are known to be translation symmetric with a certain unit cell size. Tensor networks can be employed to model these states in the thermodynamic limit by a lattice periodic contraction of tensors.

For two or three dimensions PEPS can be extended to an infinite (iPEPS [12]) variant in which the state of the system is described by an infinitely repeating pattern of PEPS tensors. The size of the repetition is referred to as the unit cell of the iPEPS. In contrast to finite size systems, these iPEPS states do not include finite size effects and are thus better suited to model bulk properties, although they are still limited by their finite bond dimension. An illustration of iPEPS with different unit cells can be found in Fig. 2.7.

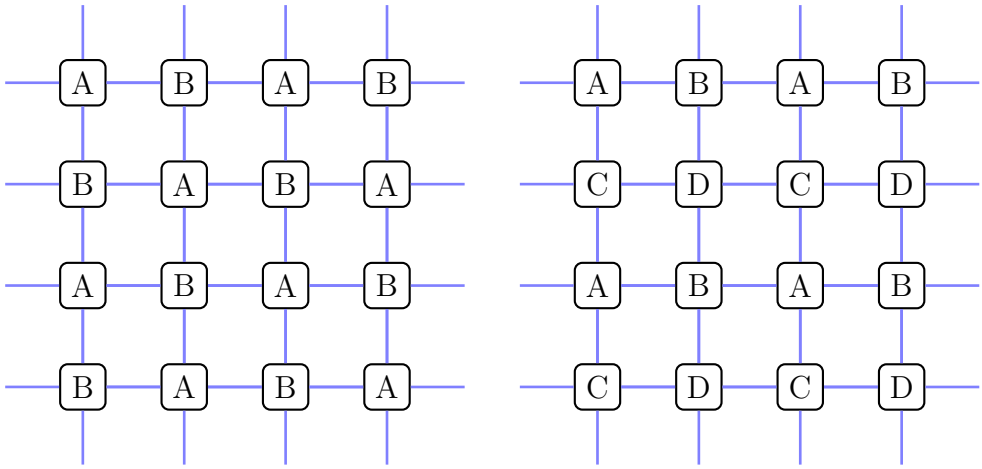

Figure 2.7: (a): Square iPEPS with a 2-site unit cell. (b) Square iPEPS with block 4-site unit cell.

To construct an iPEPS ansatz for a lattice, tensors are usually placed at the lattice sites and contracted along nearest neighboring tensors. Alternatively, multiple sites can be contracted together in a coarse-graining ansatz. This can be advantageous as the coarse-grained tensor can describe correlations of sites within it exactly but at the same time increases the physical dimension of the tensor exponentially in the number of single coarse-grained sites.

When searching for ground states of a model on a lattice, the chosen iPEPS unit cell has to be commensurate with the primitive unit cell of the ground state. Generally, the ground state energies are not equal for different choices of unit cells and multiple configurations have to be compared to find a unit cell truthfully representing the ground state symmetry of the model.

Ground states for a Hamiltonian with different model parameters, like an external magnetic field, might show different translation symmetry, indicating a phase transition. Therefore different possible unit cells have to be investigated independently for different parameters.

2.2.7 Projected Entangled Simplex States (PESS)

Projected entangled pair states describe quantum states by correlating entanglement in pairwise relations between site tensors. In some cases, such as frustrated antiferromagnetic systems, entanglement is found to be correlated between larger groups of sites and PEPS have been found to have trouble representing these correlations through pairwise relations and updates.

Projected entangled simplex states [17] (PESS) are a generalization of PEPS describing a quantum state on a lattice with a network of two kinds of tensors. Physical site tensors sit on the lattice sites and represent their physical degrees of freedom (c.f. Fig. 2.8). Multiple physical tensors are connected by simplex tensors modeling the mutual correlations between the connected sites. This structure aims to better capture the entanglement structure in lattices with magnetic frustration resulting from odd numbered antiferromagnetic nearest neighbor interactions like found in the Kagomé lattice [16].

2.3 Calculating Expectation Values

To obtain physical information about the quantum states modeled by tensor networks, we need the ability to obtain expectation values of relevant physical observables, for example the per site energy or magnetization.

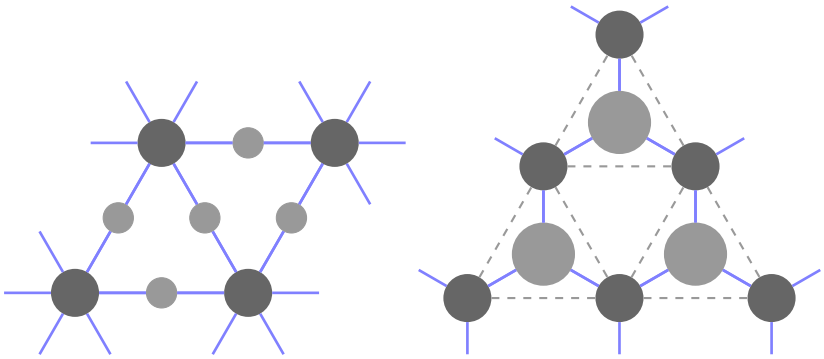

(a) (b)

Figure 2.8: (a) PEPS state in bond matrix representation on the triangular lattice. (b) 3-PESS state on a triangular lattice. The dark circles are site tensors and the brighter ones are (a) bond matrices / (b) simplex tensors.

The exact calculation of expectation values from PEPS by contraction of the full network is unfortunately very expensive and impossible for infinite PEPS. To mitigate this problem a series of approaches and methods for approximate calculation of expectation values have been developed over the years such as boundary MPS [12], corner transfer matrix renormalization group [32] (CTMRG) and tensor renormalization group [13] (TRG). These approaches are justified in so far as approximate calculation of ground state expectation values have been shown to be possible in quasipolynomial time [30].

We will illustrate the two methods to calculate expectation values for iPEPS states used in this thesis. The first method uses mean field environments to calculate expectation values. It is straightforward to implement, even for complex tensor network structures, and numerically cheap, but as it heavily approximates the environment it can produce inaccurate results. The other method is CTMRG, a state of the art method using higher dimensional tensors to represent the environment around a site tensor. For sufficient environment bond dimension this produces accurate expectation values, but requires significantly more computational resources, is harder to implement, and is not defined on arbitrary lattices.

2.3.1 Mean Field Expectation Values

In Section 2.2.4 we demonstrated the construction of an MPS by successive Schmidt decomposition. After each decomposition the diagonal matrices storing the Schmidt values were absorbed into the site tensors. Alternatively, the Schmidt values can remain as diagonal bond matrices in the tensor network as they contain useful information about the degree of correlations on each index. This representation of MPS is employed in the time evolving block decimation algorithm (TEBD) [33].

Analogously, PEPS can also formulated in this form (see Fig. 2.8(a)), although a the bond matrices are not real Schmidt coefficients anymore as PEPS can not be brought into canonical form. Instead the bond matrices can be seen as a mean field approximation of the environment of each site tensor.

An approximate local density matrix of e.g. two sites A, B can then be calculated by contracting two sites with the bond vector in between them. This tensor is then contracted with its complex conjugate while inserting the environment bond vectors on each contracted index as a nearest neighbor environment [34].

This yields a local mean field density matrix ρ_{AB}. As this density matrix is not in general normalized, the expectation value is calculated as

$$\langle O \rangle = \frac{\mathrm{tr}(\rho O)}{\mathrm{tr}(\rho)}. \tag{2.11}$$

See Fig. 2.9 for an illustration in tensor graphical notation.

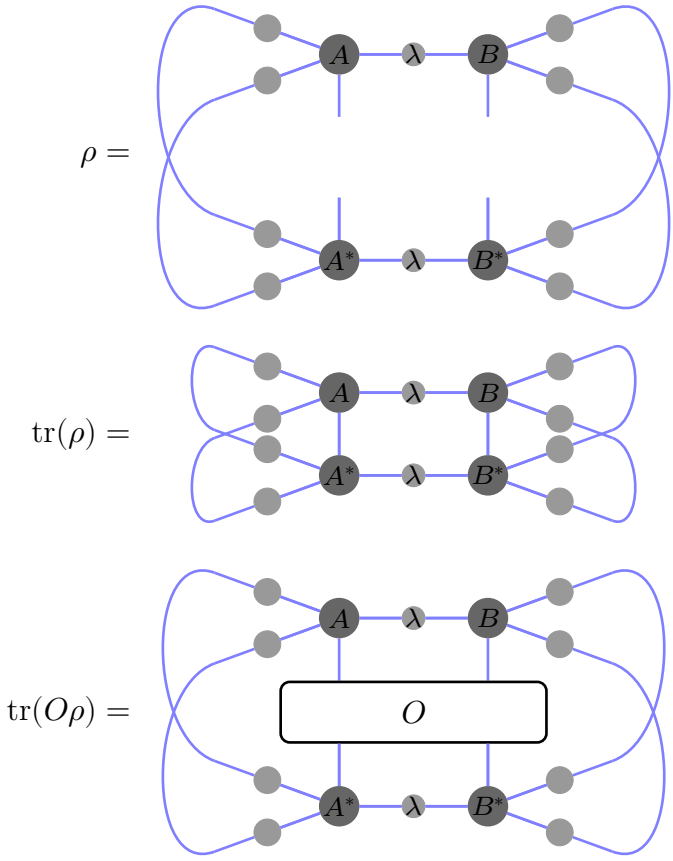

Figure 2.9: Calculating a two-site expectation value for a single bond from mean field bond matrices.

This method of obtaining expectation values is a rough approximation, potentially yielding inaccurate results, especially for large correlation lengths. As this is a local method of calculating expectation values it is easy to use, even for complex lattice structures such as the floret pentagonal lattice.

2.3.2 Corner Transfer Matrix Renormalization Group (CTMRG)

The corner transfer renormalization group (CTMRG) algorithm [32] is an iterative method using bounding corner- and transfer-tensors to calculate an effective environment of an iPEPS unit cell. This is achieved by successively absorbing parts of the unit cell into the environment, followed by coarse-graining to renormalize the dimension of the environment. Once this iterative process converges the resulting environments can be used to calculate the norm and expectation values on the iPEPS state.

CTMRG is usually applied to an iPEPS with a square lattice topology. Non-square lattices are typically mapped to a square lattice in order to use CTMRG on them, although there exists an extension of CTMRG to other lattices, e.g. the honeycomb lattice [35] and recently a range of other lattices [36].

For a square unit cell, the environment of each site tensor is described by four transfer tensors, encoding the environment in the four nearest neighbor directions of the site tensors, and four corner matrices representing the corner region between these directions. The environment bond dimension of the indices between transfer tensors and corner matrices, denoted with χ_E, is distinct from the bulk bond dimension χ_B and is usually chosen larger, as it needs to capture the correlations of the whole lattice environment. An illustration of a one site unit cell with a CTMRG environment can be found in Fig. 2.10.

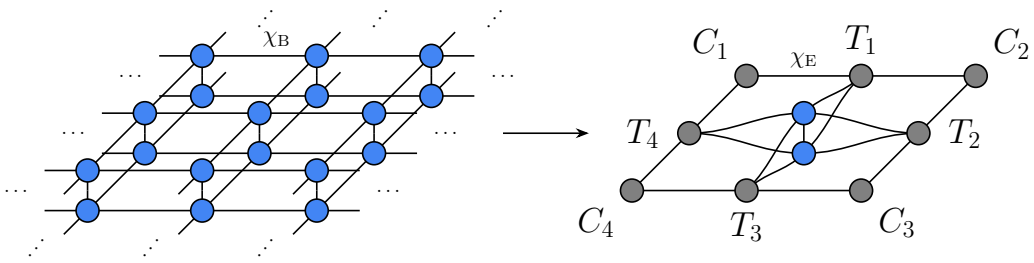

Figure 2.10: Illustration of representing the lattice environment of a site tensor double layer with a CTMRG environment. Image from Ref. [37].

To calculate the environment, the algorithm is started with randomly initiated tensors or with identity environments. For a full iteration step the CTMRG procedure of insertion, absorption and renormalization, also called a CTMRG move, is then performed in each of the four directions.

A CTMRG move in a certain direction updates the environment in that direction for each site in the PEPS unit cell. These updates are applied column-by-column for horizontal moves and row-by-row for vertical moves. E.g. for a left move the environment is updated for each site in the first column of the unit cell, then for each site of the next column until the whole unit cell has been updated.

To update the environment in a left move (illustrated in Fig. 2.11) a column of the unit cell PEPS tensors are inserted together with the top transfer tensor at the top and the bottom transfer tensor at the bottom. This inserted column is absorbed into the left environment by contracting the transfer matrices of the inserted columns with the corner matrices of the environment and the inserted sites with the transfer tensors of the left environment. With these contractions, the environment bond dimension of the contracted corner and transfer tensors grows by χ_{B}^2, requiring a renormalization step in order to keep the dimension of the environment tensors bounded.

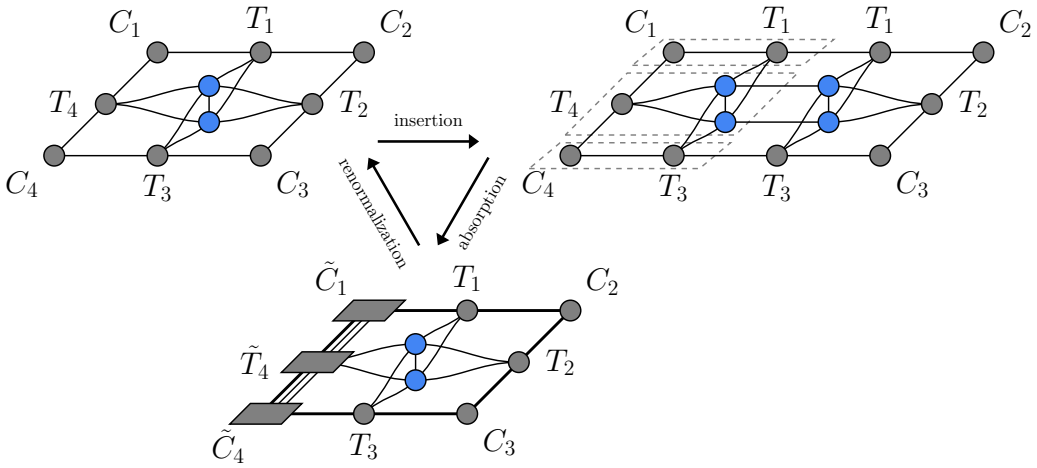

Figure 2.11: Illustration of a left CTMRG move, consisting of the insertion of a site vector, absorption into the environment and renormalization of the environment. Image from Ref. [37].

The renormalization of the environment tensors is then achieved with so called projectors, which are usually calculated from finding the optimal low-rank representation of the environment by performing an SVD on some part of the environment. The specifics of calculating projectors are beyond the scope of this thesis, partly because there are several different methods and finding well-performing projectors being an active field of research. Besides the most common full projectors [38], there are projectors calculated on half of the environment (see review [37]), as well as variants improving the numerical stability [39] and approximate approaches [40].

Once the updated environment tensors have been truncated to environment dimension χ_{E}, the procedure is repeated for the next column (for a left move) of the unit cell until the whole unit cell is processed this way. This concludes a CTMRG move in one

direction. After the CTMRG moves in each direction (left, right, top, bottom) are completed, the iteration starts anew until a fix point is reached. Whether a fix point is reached can be determined by comparing the singular values of the corner tensors.

Together with the fix-point environment in terms of corner- and transfer-tensors and the unit cell, a density matrix can be calculated and used to further compute the norm and expectation values of the iPEPS state.

The precise procedure and implementation used for CTMRG in thesis can be found in Ref. [37].

Because the used CTMRG method operates on square lattice unit cells, non-square lattices have to be mapped to a square lattice in order to apply the algorithm. This can be achieved by contracting multiple site tensors in a unit cell (coarse-graining), or splitting sites into multiple tensors via an SVD (fine graining). Later in Section 3.3.1 the floret pentagonal lattice will be mapped this way to find the ground state approximation and compute expectation values.

2.4 Finding Ground States

For most many-body models the exact eigenstates of the systems are not known, so working from an existing state and explicitly constructing it as a PEPS is not possible. On the other hand many interesting features of frustrated systems are already found at zero temperature so that understanding the ground state can give critical insights into the behaviour of a model. For tensor network states there is several methods to arrive at ground state, or rather an approximation thereof. These methods generally start from an initial (random) state and iteratively optimize this state for minimal energy, although the specifics vary.

In this section we will present two methods which will later be utilized to find the ground state of the investigated model on two dimensional tensor network ansatzes.

We will now give a brief overview of the approach and (dis-)advantages of each method:

- Simple update, based on an imaginary time evolution. This method is easy to implement, even for more complicated lattice geometries such as a PESS ansatz on the floret pentagonal lattice. As it uses a trotterized imaginary time evolution it optimizes the energy locally and thus might struggle for complex Hamiltonians with e.g. magnetic frustration where the ground state cannot be described by a subsequent local energy optimization.

- Variational update, inspired by the the variational principle, which uses the parameters of the full iPEPS unit cell as variational ansatz to optimize the tensor network state in order to find the global minimal energy. For variational update the energy of the state is evaluated with CTMRG, computing the gradient of the energy using automatic differentiation. The quantum state is then optimized using nonlinear gradient informed optimization techniques. This method has higher computational cost but optimizes the energy of the quantum state globally.

2.4.1 Imaginary Time Evolution & Simple Update

Simple update [41] is an adaptation of the infinite time evolving block decimation (iTEBD) algorithm [42] for MPS to higher dimensions. Both methods use localized evolution operators to achieve either time evolution of a quantum state or imaginary time evolution to find ground states. As we are interested in finding ground states of 2D many-body states we will focus on the latter.

We will commence by introducing the imaginary time evolution, followed by an explanation of how an approximate version can be defined in terms of local evolution operators using a Suzuki-Trotter decomposition. Subsequently, we will provide a detailed explanation of the simple update algorithm and discuss its advantages and limitations.

Trotterized Imaginary Time Evolution

One general approach to find the ground state of a quantum many-body system is imaginary time evolution. It is a power method, starting from a initial state $|\psi\rangle$, often chosen randomly and applying the time evolution operator with an imaginary time $t = i\tau$ until it converges to the eigenstate $|\psi_0\rangle$ of the lowest eigenvalue E_0

$$\begin{aligned} \mathrm{e}^{-\tau H}|\psi\rangle &= \sum_{i=0}^{n} \mathrm{e}^{-\tau H}|\psi_i\rangle = \sum_{i=0}^{n} \mathrm{e}^{-\tau E_i}|\psi_i\rangle \\ &= \mathrm{e}^{-\tau E_0}\left(|\psi_0\rangle + \sum_{i=1}^{n} \mathrm{e}^{-\tau(E_i-E_0)}|\psi_i\rangle\right) \\ &\underset{\tau\to\infty}{\propto} |\psi_0\rangle\,, \end{aligned} \tag{2.12}$$

while the states of higher eigenvalues are exponentially suppressed. Here E_i and $|\psi_i\rangle$ are the eigenvectors of the Hamiltonian H.

When working with tensor network states, applying the imaginary time evolution operator on the whole state would in general transfer the state back to a general quantum state and thus negate any cost reduction gained by using a tensor network

structure. Thus the strategy is to break down the Hamiltonian into a sum of local non-overlapping parts, e.g.

$$H = H_A + H_B \tag{2.13}$$

and to approximate the evolution by sequential evolutions of the partial Hamiltonian using a Suzuki-Trotter decomposition [43]

$$\mathrm{e}^{-\tau(H_A+H_B)} = \mathrm{e}^{-\tau H_A}\mathrm{e}^{-\tau H_B} + \mathcal{O}(\tau^2). \tag{2.14}$$

As the error of the expansion scales with the square of the imaginary time, τ is chosen to be small. To still reach convergence the evolution is iterated in small steps of $\delta\tau$ until convergence is reached (see Fig. 2.12).

Applying the Suzuki-Trotter expansion strategy on a tensor network state for a Hamiltonian with local two-body interactions, the smallest possible partition of the Hamiltonian is made of non overlapping sets of two-site evolution operators along the individual virtual bonds of the tensor network state. In order to repeat this step without increasing numerical costs on every iteration the local evolution of the state has to be renormalized into a tensor network state with the original properties (i.e. number of sites and bond dimension).

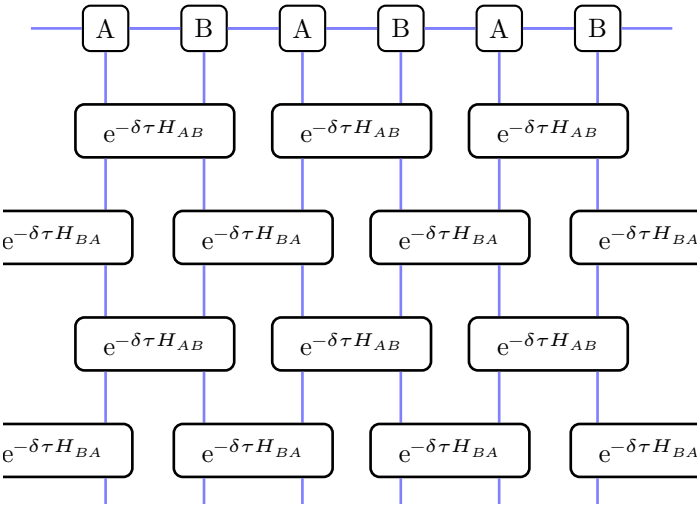

Figure 2.12: Using a Suzuki-Trotter expansion the imaginary time evolution operator $\mathrm{e}^{-\delta\tau H}$ is split into commuting gates and applied consecutively. Although this picture depicts an MPS it can analogously be viewed as a slice through a trotterized imaginary time evolution on a PEPS state.

This renormalization step has to split the updated two-site tensors back into single site tensors and discard part of the information of the tensor network state. It is therefore crucial to identity the most relevant information for the description of the physical system, discarding the least relevant parts of the state. For the finite 1D case (MPS) this distinction can be made by truncating the Schmidt coefficients along the bonds using an MPS in canonical form, leading to TEBD [44].

In the case of infinite MPS a canonical form is not possible anymore as there is no unifying way to separate the quantum state into two finite parts. But a similar scheme using bond vectors as approximate environments between sites can be formulated, leading to the infinite TEBD [42] (iTEBD) algorithm.

Simple Update Algorithm

For the 2D systems we are interested in, we face the same issue of lacking a canonical form, which means not having access to normalizing the quantum state by truncating Schmidt coefficients.

Analogous to iTEBD in 1D, simple update [41] is an adaption of the method for infinite PEPS, describing the quantum state with both site tensors Γ_i and diagonal bond matrices λ_{ij}, using the latter to approximate the environment between site i and its neighboring site j in a mean field approach. The simple update method is very fast compared to more accurate methods (e.g. fast full update [45], variational optimization [46]), but the mean field environment can only capture a rather limited amount of environment entanglement with the environment. Therefore the method has problems finding the ground state for highly correlated systems.

Nevertheless, for non critical, gapped systems with short correlation lengths the method often leads to adequate approximate results. At the same time it is straightforward to implement, compared to more rigorous methods.

We will now give step-by-step explanation of the simple update algorithm using the example of a square lattice iPEPS with a checkerboard $\left(\begin{smallmatrix} a & b \\ b & a \end{smallmatrix}\right)$ unit cell. An accompanying tensor diagram of the algorithm procedure can be found in Fig. 2.14.

In this example the PEPS state consists of two site tensors and four bond matrices (see Fig. 2.13). One whole iteration of the algorithm consists of updating the tensors once along each bond tensor where in each update step one bond-vector λ and two site tensors A and B are updated by an imaginary time evolution operator.

After updating each bond, the convergence is checked by comparing the norm of the difference of the old and new λ matrices. The update step of the bonds is iterated until convergence is reached.

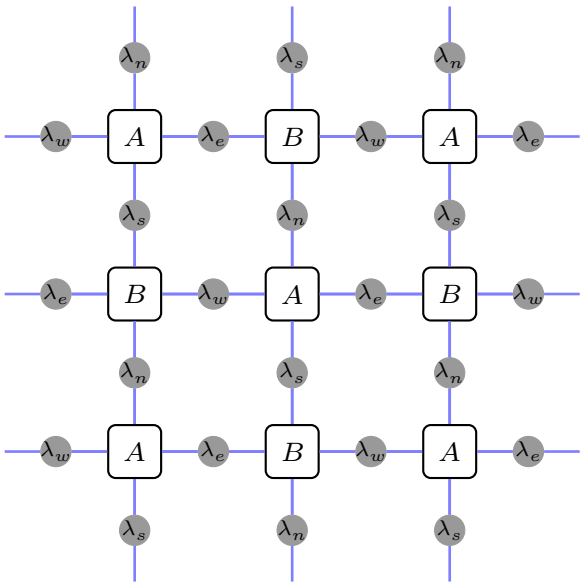

Figure 2.13: Tensor diagram of a bond matrix iPEPS state with an AB unit cell.

In a first step the bond matrices which are adjacent to the site tensors but not the updated bond λ will be absorbed to the site tensors as an approximated mean field environment.

For a checkerboard-square iPEPS, we have 4 different bonds which we can label n, w, s, e. Contracting the environment matrices for site tensors A, B and bond e would look like

$$\begin{aligned} \tilde{A}_{n,w,s,e,p} &= \sum_{n',w',s'} A_{n',w',s',e,p}\ \lambda^{n}_{nn'}\lambda^{w}_{ww'}\lambda^{s}_{ss'} \\ \tilde{B}_{n,w,s,e,p} &= \sum_{n',w',s'} B_{n',w',s',e,p}\ \lambda^{n}_{nn'}\lambda^{w}_{ww'}\lambda^{s}_{ss'}. \end{aligned} \tag{2.15}$$

After contracting the auxiliary environment matrices, the evolution operator is contracted with the site tensors yielding a tensor S with the bond indices of the adjacent bonds of A and B as well as their physical indices. The tensor is reshaped into a matrix M_S with indices originating on A's side on the first index and B's indices on the other one.

Next an SVD is applied on the matrix, yielding a product of unitary matrices U, V and the diagonal singular value matrix Σ

$$M_S = U\Sigma V^{\dagger}. \tag{2.16}$$

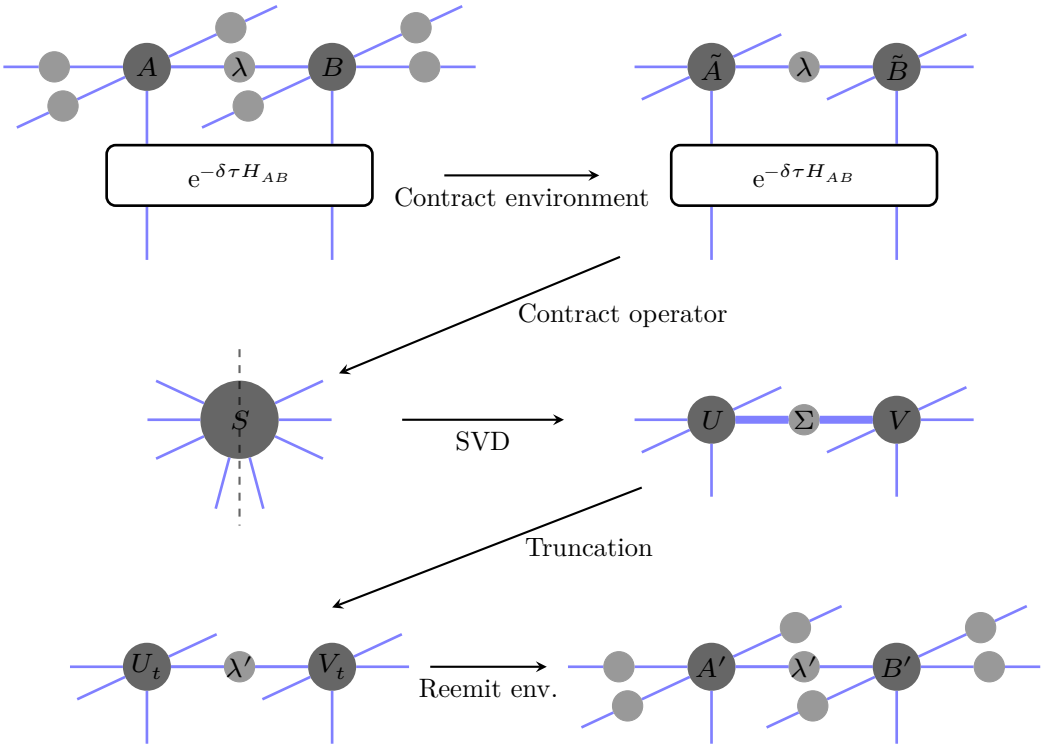

Figure 2.14: Illustration of a simple update step of sites A and B along bond λ. The substeps of the algorithm are:

- The bond matrices of surrounding bonds are absorbed into the site tensors A and B.
- The trotterized imaginary time evolution operator $\mathrm{e}^{-\delta\tau H_{AB}}$ is contracted with the site tensors, yielding a large tensor S containing the physical indices of both lattice sites.
- S is decomposed along the updated bond by an SVD: $M_S = U\Sigma V^\dagger$.
- The lowest singular values in Σ are truncated, leaving the largest χ_B values.
- The bond matrices of the neighboring bonds are re-emitted by contracting U and V by their inverse, concluding one update step.

After this step the number of diagonal entries in Σ will be $\chi_{\mathrm{B}}^{c-1}p$, where c is the number of bonds of a site. In order to keep the dimension of the tensors bounded, we project the resulting tensor into the relevant subspace in terms of entanglement correlations, determined by the largest singular values. The dimensions of the lower singular values are truncated from U,V and Σ to the chosen bond dimension χ_{B}. The truncated U and V are identified as the new site tensors.

After normalization to improve numerical stability the truncated Σ is the new bond matrix λ. We want to note that although the singular values are normalized in this step, in general the whole state represented by the tensor network structure does not have to be normalized. This has to be accounted for while calculating expectation values later.

As last part of the update step the bond matrices of the neighboring, not updated bonds are recovered by reemitting them from the update site tensors

$$\begin{aligned}\tilde{A}_{n,w,s,e,p} &= \sum_{n',w',s'} \tilde{U}_{n',w',s',e,p}\ \frac{1}{\lambda^{n}_{nn'}\lambda^{w}_{ww'}\lambda^{s}_{ss'}} \\ \tilde{B}_{n,w,s,e,p} &= \sum_{n',w',s'} \tilde{V}_{n',w',s',e,p}\ \frac{1}{\lambda^{n}_{nn'}\lambda^{w}_{ww'}\lambda^{s}_{ss'}},\end{aligned} \tag{2.17}$$

where $\tilde{U}$ and $\tilde{V}$ are the tensors obtained by reshaping the truncated U and V matrices.

For performance reasons, after contracting the environment matrices, the site tensors are split with a QR-decomposition and the steps until reemitting the environment matrices are applied on the R matrices (c.f. Ref. [34, Fig. 2]).

Using this optimization the computational cost of the algorithm is dominated either by the QR decomposition which scales with $\mathcal{O}\big(\chi_{\mathrm{B}}^{c+1}p^2\big)$, where c is the coordination number of the lattice tensors, or by the SVD with a complexity of $\mathcal{O}(\chi_{\mathrm{B}}^3 p^3)$.

Because the simple update algorithm works by locally updating only two neighboring tensors it can be implemented for arbitrary lattice geometries [34]. On the other hand, as a method which updates energies locally, it will struggle with complex Hamiltonians, like models with magnetic frustration, where the global energy minimum usually differs from the local minima. One approach to ameliorate this issue, is to adept the simple update to a PESS tensor network structure [17] using a higher order SVD [47]. Here all lattice site tensors connected to a simplex tensor are updated at once, instead of the pairwise updates. This enables a better evolution of the state because it optimizes units of frustrated spins instead of pairs, at the disadvantage of higher computational and memory costs.

2.4.2 Variational Update

Another approach to find or more precisely setting upper bounds on the ground state energies is to use variational methods which optimize a state $|\psi(\mathbf{x})\rangle$ to find the minimal energy depending on the parameter space $\mathbf{x}$.

This principle is rooted in the fact that by definition the energy of any conceivable quantum state remains at or above the ground state energy level.

$$\forall \psi : \; E_0 \leq \frac{\langle \psi | H | \psi \rangle}{\langle \psi | \psi \rangle}. \tag{2.18}$$

Variational methods are a well established approach in tensor network methods, particularly the DMRG [10] algorithm for matrix product states. By regarding the tensor entries as variational parameters, a tensor network state becomes a parameterized state which is to be optimized globally by tuning the tensor entries. The larger dimensionality and more complex geometry inherent in two-dimensional systems result in an expanded parameter space for PEPS, making optimization considerably more challenging. As a consequence, variational methods for 2D tensor networks have gained popularity only relatively recently compared to MPS.

Optimization of nonlinear functions on large parameter spaces profits greatly from having access to gradient information. First approaches in variational optimization of PEPS states [46, 48] constructed these gradients manually and demonstrated the potential of variational methods in 2D. However explicitly constructing gradients by hand is tedious, error prone and does not generalize well for different models or lattices.

Modern advances in the application and implementation of automatic differentiation, driven by breakthroughs in machine learning, allow programmers to write algorithms with access to gradient information without the need for explicit differentiation programming. Recently, automatic differentiation has found application in calculating gradients for variational optimization of PEPS [49, 37].

The general strategy in this approach is to evaluate the energy of a PEPS state by CTMRG and to then use automatic differentiation to calculate the gradient of the energy with respect to the PEPS tensors. With the computed gradient, optimization methods such as nonlinear conjugate gradient descent, the Broyden–Fletcher–Goldfarb–Shanno algorithm (BFGS) and limited-memory BFGS (L-BFGS) can be used to calculate a descent direction and line search methods considering Armijo or Wolfe conditions are used to determine a suitable step size. After each update step the energy is again computed in a full CTMRG sweep and the next update step is performed. This is iterated until some measure of convergence is reached, typically measured by the norm of the gradient.

In contrast to DMRG or simple update the variational update method calculates the gradient of a full iPEPS unit cell and its CTMRG environment, thus searching for the global energy minimum of the state. Although the method searches for a global minimum the optimization can still get stuck in local minima. In this case the tensor network can be perturbed by random noise to lift it out of the local minimum.

As the variational method uses CTMRG to compute the energy it takes account for the whole environment of the site tensors, although still limited by the environment bond dimension χ_{E}. Due to this better approximation of the infinite environment and because it optimizes the energy globally instead of locally, it produces superior results in estimating ground states compared to simple update [37]. Nonetheless, these benefits entail significantly higher computational costs and memory requirements.

2.5 Correlation Length

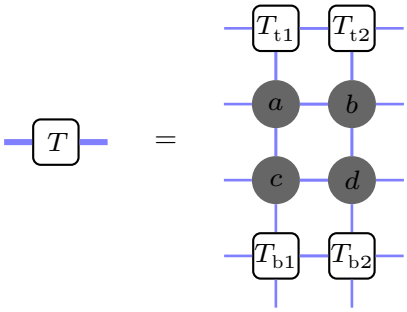

Figure 2.15: Example of a horizontal transfer matrix for a four site $\left(\begin{smallmatrix} a & b \\ c & d \end{smallmatrix}\right)$ unit cell.

We use infinite PEPS to approximately represent infinite lattices and CTMRG to further approximately calculate expectation values of observables using a finite environment. Despite these approximations, the goal is to obtain information about an infinite bulk lattice, where theoretically correlations could be arbitrary long, and indeed iPEPS can represent correlations of arbitrary length at finite bond dimensions [31]. The finite CTMRG environment on the other hand imposes a restriction to the maximally representable correlation length. This restriction in general jointly depends on the PEPS bond dimension χ_{B} and environment bond dimension χ_{E} [50].

This maximal correlation length can be determined by regarding the double-layer unit cell and CTMRG transfer matrices as a whole transfer matrix [51] for either vertical or horizontal direction (see Fig. 2.15).

Repeatedly applying this transfer matrix gives an exponentially decaying contribution for all but the dominant eigenvector to the largest eigenvalue λ_0, where the characteristic correlation length can be obtained from the largest and the second largest

eigenvalue λ_1 as

$$\xi = -\frac{1}{\ln(|\lambda_1|) - \ln(|\lambda_0|)}. \tag{2.19}$$

This can be seen by applying the transfer matrix T to a vector $\mathbf{v}$ and expanding in the eigenvectors $T\mathbf{v}_i = c_i\mathbf{v}_i$ of the transfer matrix

$$\begin{aligned} T\mathbf{v} &= T\sum_{i=0}^{N} c_i\mathbf{v}_i = \sum_{i=0}^{N}\lambda_i c_i\mathbf{v}_i \\ &= \lambda_0\left(c_0\mathbf{v_0} + \sum_{i=1}^{N}\frac{\lambda_i}{\lambda_0}c_i\mathbf{v_i}\right) \\ T^n\mathbf{v} &= \lambda_0^n\left(c_0\mathbf{v_0} + \sum_{i=1}^{N}\left(\frac{\lambda_i}{\lambda_0}\right)^n c_i\mathbf{v_i}\right) \\ &= \lambda_0^n\left(c_0\mathbf{v_0} + \sum_{i=1}^{N}\mathrm{e}^{-n\ln\left(\frac{\lambda_0}{\lambda_i}\right)}c_i\mathbf{v_i}\right) = \lambda_0^n\left(c_0\mathbf{v_0} + \sum_{i=1}^{N}\mathrm{e}^{-\frac{n}{\xi_i}}c_i\mathbf{v_i}\right). \end{aligned} \tag{2.20}$$

Eq. (2.20) shows, that even though our representation of the lattice is infinite, correlations lengths of computed expectation values are still bounded by the finite environment. Usually higher correlation lengths can be reached with higher bond dimensions χ_B and particularly with higher environment bond dimension χ_E.

When simulating quantum states using tensor network methods we are limited to inspect states at finite bond dimension, (usually) approximating the physical quantum states. One effect of this limitation is the introduction of a finite length scale which can be quantified by the correlation length ξ. To infer properties about the physical state it is sensible to extrapolate the results obtained using states with restricted (environment) bond dimension to the limit of $\xi \to \infty$ where no length scale restriction is imposed [52].

3 Investigation of the Floret Pentagonal Lattice

In this chapter we will investigate the Heisenberg antiferromagnet Hamiltonian on the floret pentagonal lattice as an example of frustrated magnetism on pentagonal lattices. This model consists of spin-$\frac{1}{2}$ particles placed on each lattice site, which interact magnetically by their mutual alignment. As we consider an antiferromagnetic model, opposite alignment of spins is energetically favoured. Because of the pentagonal structure of nearest neighbors in the lattice it harbors geometrical frustration: Spins can not align opposite to all their neighbors. Most existing research in frustrated quantum magnetism has been focused on lattices made up of triangles of frustrated pairs, like the Kagomé and triangular lattices. No material bearing the structure of the floret pentagonal lattice has been found to date. Still, the lattice can serve as a model to better understand magnetism in lattices with frustrated clusters of more than three sites.

Using the introduced tensor network methods, we set out to compute important properties such as the ground state energy and magnetization and will investigate how these properties behave under different magnetic field strengths.

We start out by detailing the properties of the floret pentagonal lattice and defining the model Hamiltonian with its free parameters. Then we will discuss the simulation and investigation of the model using two methods introduced earlier: The simple update method and the variational update method.

3.1 Model

In this section we describe the model we want to investigate, the antiferromagnetic Heisenberg model on the floret pentagonal lattice. We start by describing the floret pentagonal lattice and its geometry and symmetry. Following this, we introduce the quantum Heisenberg model and discuss how interaction ratios relate to the lattice structure. In the end of this section we will give a brief summary of previous studies of the Heisenberg model on the floret pentagonal lattice.

3.1.1 Lattice

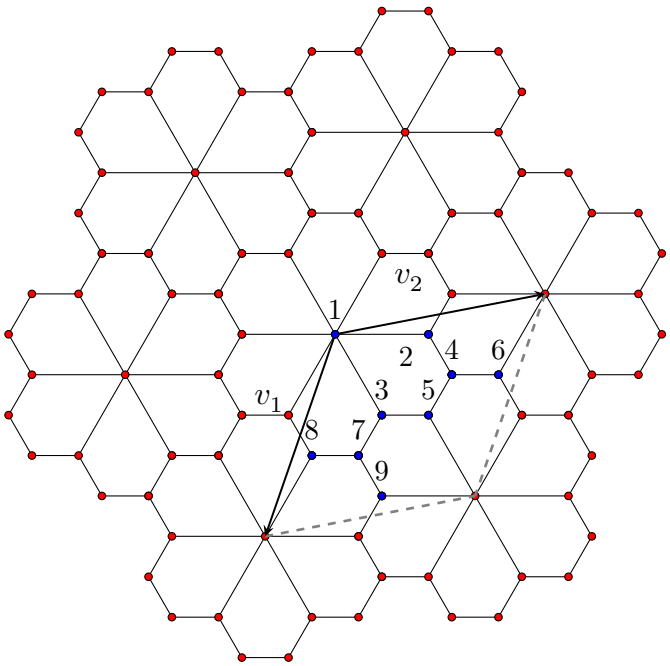

Figure 3.1: Structure of the floret Pentagonal lattice. The sites are indicated with red dots, black lines show nearest neighbors. The two arrows show the hexagonal lattice vectors and the sites contained in a unit cell are indicated in blue.

The floret pentagonal lattice, as shown in Fig. 3.1, is a lattice structure based on the hexagonal Bravais lattice with a basis of nine sites, the basis vectors of which can be found in Table 3.1. The lattice vectors of the lattice are

n	1	2	3	4	5	6	7	8	9
$2\frac{x}{a}$	0	4	2	5	4	7	1	-1	2
$2\frac{y}{a}$	0	0	$-2\sqrt{3}$	$-\sqrt{3}$	$-2\sqrt{3}$	$-\sqrt{3}$	$-3\sqrt{3}$	$-3\sqrt{3}$	$-4\sqrt{3}$

Table 3.1: Basis vectors of the floret pentagonal lattice in terms of the nearest neighbor lattice constant a.

$$v_1 = \frac{a}{2}\begin{pmatrix} 9 \\ \sqrt{3} \end{pmatrix}, \tag{3.1}$$

$$v_2 = \frac{a}{2}\begin{pmatrix} 3 \\ -5\sqrt{3} \end{pmatrix}, \tag{3.2}$$

where a is the lattice constant.

The lattice is originally known as the *floret pentagonal tiling* and has been studied as a periodic tiling. The symmetry group of the tiling is the wallpaper group $p6$, which has three rotation centers with respective orders of 6, 3 and 2. The lattice can be seen to be made up of irregular pentagons, "petals", arranging in hexagonal "flowers" tiling the plane (see Fig. 3.2).

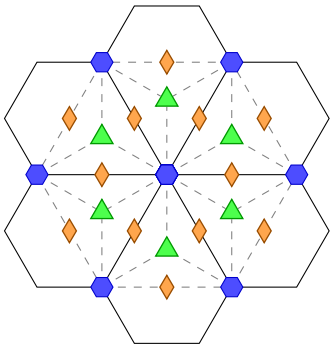

Figure 3.2: The $p6$ symmetry group displayed on a "flower" of the floret pentagonal lattice. The symbols indicate the three rotation centers: sixfold ⬣, threefold ▲, twofold ⧫.

We identify three geometrically different types of sites in the lattice, which we will label with A, B and C. One unit cell (marked blue in Fig. 3.1) contains a single Type A site (site 1), six sites of Type B (sites 2, 3, 5, 6, 8, 9) and three sites of Type C (sites 4 and 7).

3.1.2 Model Hamiltonian

The target model of our investigation is the spin-$\frac{1}{2}$ Heisenberg model antiferromagnet (AFM) with nearest neighbor interactions, composed of an interaction term and the Zeeman term for an external magnetic field along the z-axis. The Heisenberg model is also known as the XXX-model, where XXX signifies that the interaction constants are equal for all three spin components (SU(2)-symmetric).

The model Hamiltonian is given by

$$H = H_{\mathrm{AF}} + H_{\mathrm{Field}} \tag{3.3}$$

$$= \sum_{\langle ij \rangle} J_{ij}\, \mathbf{S}_i \cdot \mathbf{S}_j - h_z \sum_i S_i^z, \tag{3.4}$$

where $\mathbf{S}_i$ are the spin-$\frac{1}{2}$ operators, $\langle ij \rangle$ denotes the pairs of nearest neighbors and the coupling constant $J_{ij} > 0$ for an antiferromagnet can depend on the type of the neighboring sites i and j (see Fig. 3.3). $h_z > 0$ is the strength of the magnetic field along the z-axis.

To understand the interactions in the Hamiltonian it is illustrative to look at the eigenstates and energies of the individual contributions.

In the Zeeman term H_{Field} the eigenstates for S_i^z are $|\uparrow\rangle$ and $|\downarrow\rangle$ at site i with energies of $\pm\frac{1}{2}$. So in our model the Zeeman term with positive h_z will favor upwards facing spins.

For the antiferromagnetic term H_{AF} the spin-spin interaction $\mathbf{S}_i \cdot \mathbf{S}_j$ can be expressed of the total spin of the sites $\mathbf{J}_{ij} = \mathbf{S}_i + \mathbf{S}_j$. Expressing the interaction in terms of the spin operators and the squared total angular momentum operator $J_{ij}^2 = (S_i + S_j)^2$

$$\mathbf{S}_i \cdot \mathbf{S}_j = \frac{\mathbf{J}_{ij}^2}{2} - \frac{\mathbf{S}_i^2}{2} - \frac{\mathbf{S}_j^2}{2} = \frac{\mathbf{J}_{ij}^2}{2} - \frac{3}{4}, \tag{3.5}$$

we see that for this term the minimal energy $-\frac{3}{4}$ is reached for a state with zero total spin, the singlet state $|\uparrow\downarrow\rangle - |\downarrow\uparrow\rangle$. The triplet states have $J^2 = 2$, resulting in an energy of $\frac{1}{4}$.

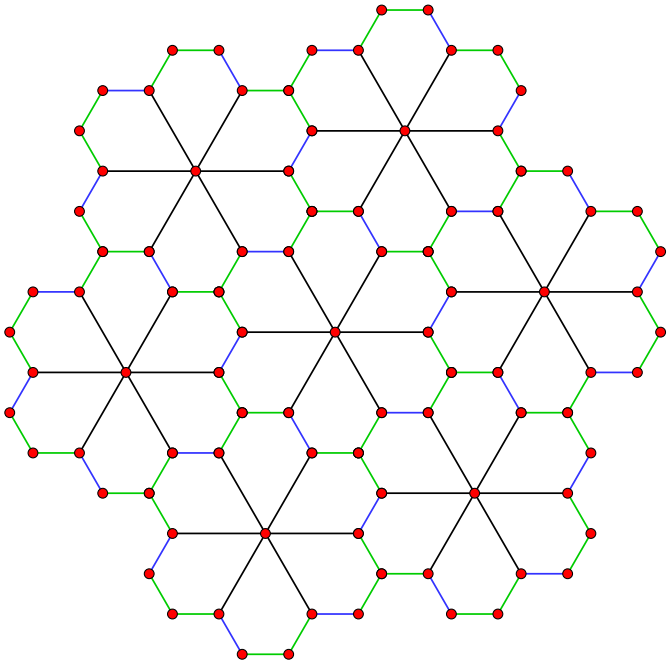

Figure 3.3: Floret Pentagonal lattice with different bond types marked by colors: Type A ↔ Type B: black, Type B ↔ Type B: blue, Type B ↔ Type C: green.

Due to the geometry of the lattice, we identify three different types of interactions which are marked in Fig. 3.3 by the colors black, green and blue. Here black bonds refer to type A ↔ type B interactions with coupling constant J_1. Blue bonds (type B ↔ type B) and green bonds (type B ↔ type C) are of the same distance in the lattice so we assign both the coupling constant J_2.

As a reference we fix the coupling strength of the black bonds $J_1 = 1$. This leads to two free parameters of our model Hamiltonian, $\eta = \frac{J_2}{J1}$ and h_z.

3.1.3 Unit Cell

In order to simulate a lattice periodic quantum state we have to decide on a unit of periodicity, the unit cell. The simplest unit cell is just the primitive unit cell of the lattice consisting of nine spins, but it not always encodes the true translational symmetry of the ground state of a given Hamiltonian. In this case, the state spontaneously breaks lattice translation symmetry, which is for instance the case for the ground state of an antiferromagnetic square lattice Heisenberg model, which has a unit cell of two sites in a checkerboard pattern [53, p. 96].

In the scope of this thesis we considered the unit cells

$$\mathcal{L}_9 = (a), \quad \mathcal{L}_{18} = \begin{pmatrix} a & b \\ b & a \end{pmatrix}, \quad \mathcal{L}_{27} = \begin{pmatrix} a & b & c \\ b & c & a \\ c & a & b \end{pmatrix} \quad \text{and} \quad \mathcal{L}_{36} = \begin{pmatrix} a & b \\ c & d \end{pmatrix}. \tag{3.6}$$

Each element in $\mathcal{L}_i$ denotes an elementary unit cell of nine spins on the floret pentagon lattice, and the matrix structure defines the PEPS unit cell in direction of the two lattice vectors. The subscript refers the total number of independent spins in each ansatz.

These unit cells where selected as they are common patterns in frustrated spin lattices. While larger unit cells being more suitable to represent the true ground state of the model can not be ruled out, they are out of reach for numerical consideration due to the high computational cost of their simulation exceeding resource constraints.

In practice finding the right unit cell for a given lattice and Hamiltonian involves trying out plausible candidates and determining which of them has the lowest ground state energy. The ground state simulation of a larger unit cell reducing to the symmetry of a smaller unit cell can be seen as an indication of the smaller unit cell being a good candidate to represent the ground state.

3.1.4 Previous Results

The antiferromagnetic Heisenberg model on the floret pentagonal lattice has been previously studied by exact diagonalization of the Hamiltonian on various finite size clusters of the lattice using Lanczos methods [20, 21].

In these studies the cluster sizes of $N = \{9, 18, 27, 36\}$ sites have been investigated for multiple values of η. The ground state energies reported for $\eta = 1$ are listed in Table 3.2.

N	9	18	27	36
E_0	-0.4839	-0.5122	-0.5001	-0.5033

Table 3.2: Exact diagonalization energy per site for finite clusters of N sites and $\eta = 1$, given in terms of the coupling constant J_1, as reported in Ref. [20].

Varying the external field h_z in z-direction, the study found magnetization plateaus at average relative z-axis magnetizations $\overline{m_z}/m_\mathrm{s} = \frac{7}{9}$ in the range of $0.55 < h_z < 1.54$ and $\overline{m_z}/m_\mathrm{s} = \frac{3}{9}$ in the range of $2.07 < h_z < 3.64$. Here $\overline{m_z}$ refers to the average site magnetization along the z-axis and $m_s = \frac{1}{2}$ to the saturation magnetization.

3.2 Investigation using Simple Update

Our first approach to simulate the model was using the natural structure of the lattice to guide the tensor network structure, representing each site with a tensor and contracting site tensors along interaction. Because it can be easily implemented for arbitrary lattice structures [34] we chose the simple update method to search for the ground state in this representation.

In this section, we describe the iPEPS and iPESS ansatzes utilized in our simulations. We then detail the simulation procedure for reproducibility and present the results. Finally, we discuss challenges encountered in calculating precise CTMRG expectation values for the simulated states.

3.2.1 iPEPS & iPESS Ansatz

For simulations using simple update we considered two ansatzes: A simple iPEPS ansatz which could be scaled to high bond dimensions and an iPESS ansatz, enabling the update of multiple sites in a frustrated cluster simultaneously.

Our iPEPS ansatz for the floret pentagonal lattice follows the nearest neighbors interactions and is congruent with the structure shown in Fig. 3.1. In this setting, the red sites correspond to site tensors and diagonal bond matrices are placed on the black edges. With the physical dimension p and the bond dimension χ_B, a primitive unit cell of the tensor network contains eight site tensors with three bond indices of dimension $p\chi_\mathrm{B}^3$, one site tensor with 6 bond indices of dimension $p\chi_\mathrm{B}^6$, and 15 diagonal bond matrices of dimension χ_B.

For iPESS a natural ansatz is placing the simplex tensors at the sites of the dual of the lattice. In the case of the floret pentagonal lattice this means placing simplex tensors at the center of each pentagon and connecting it with each of the sites sitting

at the corners. This structure resembles an overlay of the floret pentagonal lattice with its dual, the snub trihexagonal lattice, as shown in Fig. 3.4. A primitive unit cell of the iPESS ansatz consists of the nine site tensors with the same dimensionality as found in the iPEPS ansatz and six simplex tensors of dimension χ_B^5 with each of the five indices connecting to a site tensor.

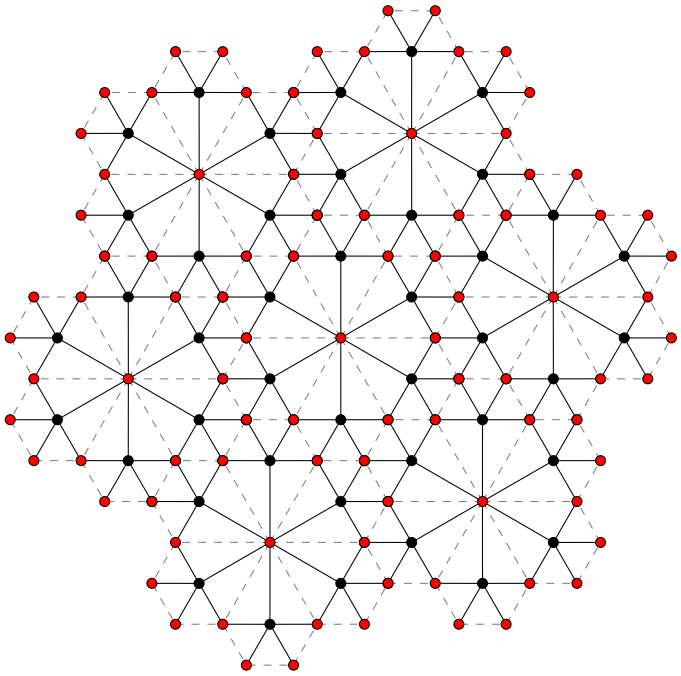

Figure 3.4: Structure of the dual iPESS ansatz for the floret pentagonal lattice. Simplex tensors are placed in the center of the pentagons. Site tensors are depicted with red dots, simplex tensors with black dots and the dashed gray lines indicate nearest neighbor relations.

3.2.2 Results

Simulation

Simple update simulations were run using a self written Julia package [54], utilizing the *TensorOperations.jl* library [55] for tensor contractions and computation of optimal contraction order.

In both the iPEPS and iPESS ansatz simulation followed the following scheme: Site tensors were initialized with random data, bond matrices and simplex tensors were initialized with identity. Imaginary time evolution starts with a trotter time step $\delta\tau_0 = 0.1$ and is run until convergence of the singular values in the bond matrices /

simplex tensors, sequentially updating along each bond vector / simplex tensor. After converging for a set $\delta\tau$ the time step is divided by 10 and a new update iteration is started. This proceeds until a minimum trotter time step of $\delta\tau_{\text{min}} = 10^{-5}$, after which the simulation process is considered converged.

Simulations for higher bond dimensions were started with the converged states of the previous bond dimension.

Simulations with iPEPS Ansatz

We ran simple update simulations with the iPEPS ansatz for all unit cell structures listed in Eq. (3.6). Convergence could not be reached for bond dimensions larger than $\chi_{\text{B}} = 2$ in several independent runs for various interaction constants η.

This indicates a problem in capturing the structure of the frustrated ground state using two-site updates. Optimizing only two states struggles to capture the dilemma of trying to align clusters of interacting spins against each other. This is a well known problem and was a motivation in developing the PESS method [17].

Simulation with iPESS Ansatz

In contrast to the iPEPS ansatz the imaginary time evolution with the iPESS ansatz generally converged for all tested bond dimensions.

We choose to investigate the model at interactions parameters $\eta \in \{1.0, 1.44, 1.56, 2.0\}$, which were also studied in Refs. [20, 21].

In this discussion of the results from the iPESS simulations, we first examine the process of identifying the most suitable unit cell at $h_z = 0$ and present the corresponding ground state energies. Following this, we present the results obtained for different magnetic field strengths. Finally, we discuss these results and address the limitations in accuracy associated with the mean field expectation values used in computing energy and magnetization.

To determine the ground state unit cell at no magnetic field we ran simulations for $\chi_{\text{B}} = 7$ and compared their energies using mean field expectation values. Best results were achieved for $\mathcal{L}_{18}$ and $\mathcal{L}_{36}$, while $\mathcal{L}_9$ and $\mathcal{L}_{27}$ displayed higher energies. As $\mathcal{L}_{36}$ can represent a $\mathcal{L}_{18}$ unit cell we conclude that $\mathcal{L}_{18}$ is the most suited to study the ground state at no magnetic field.

The obtained ground state per-site energies for bond dimension $\chi_{\text{B}} = 7$ and different η can be found in Table 3.3.

A plot of the energies for inverse bond dimensions can be found in Fig. 3.5. For all η the energies indicate convergence for increasing bond dimension.

η	1.0	1.44	1.56	2.0
$E_0(\chi_\mathrm{B} = 7)$	-0.383	-0.506	-0.540	-0.669

Table 3.3: Energy per site for different values of η, calculated using mean field expectation values on PESS states obtained by simple update with bond dimension $\chi_\mathrm{B} = 7$.

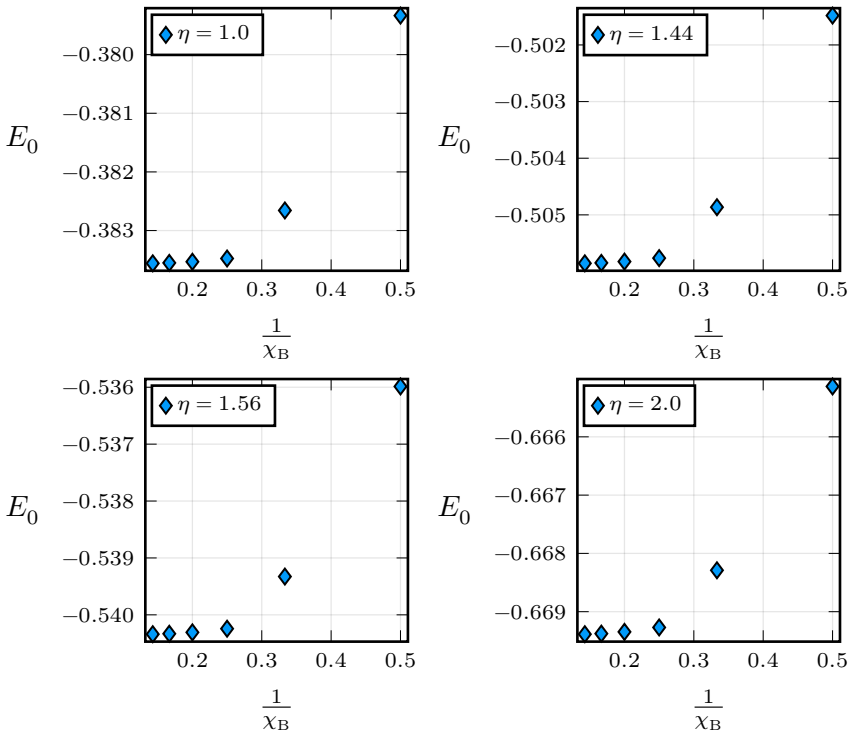

Figure 3.5: Mean field per-site ground state energies of the PESS simulations for $\eta \in \{1.0, 1.44, 1.56, 2.0\}$.

To obtain data for a magnetization curve simulations were run at bond dimension $\chi_B = 5$, with the external magnetic field h_z being varied from 0 to 5 in steps of 0.25.

The staggered magnetizations for $\chi_B = 7$ and $h_z = 0$ was calculated using mean field expectation values to be $\overline{m^s}/m_s \approx 0.84$ for all values of η. A plot of the average relative z-axis magnetization $\overline{m_z}/m_s$ over the field strength h_z can be found in Fig. 3.6.

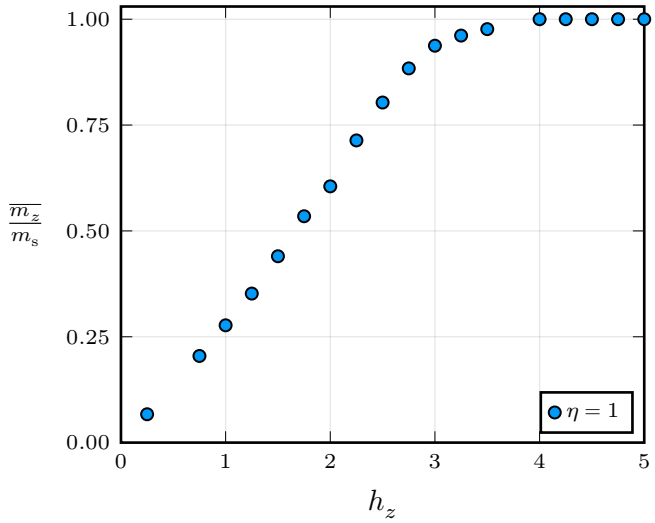

Figure 3.6: Average relative z-axis magnetization $\overline{m_z}/m_s$ dependent on external field strength h_z at $\eta = 1$. The magnetization was calculated using the mean field expectation value method.

Comparing the energies to the ED results from Refs. [20, 21], where for $h_z = 0$ and the 36-site unit cell a ground state per-site energy of $E_0^{N=36} = -0.503$ was reported at $\eta = 1$, our results show significantly higher energies.

The obtained staggered magnetizations at $h_z = 0$ are untypically high and the magnetization curve bears no resemblance to the results of the exact diagonalization study, showing none of reported magnetization plateaus.

These discrepancies could be rooted in two reasons. On the one hand, simple update, while often producing adequate results, is known to not always being able to converge close to the actual ground state. On the other hand, the energy expectation values were calculated using the mean field expectation value method. This method is a very strong approximation and can produce inaccurate results (discussed in Ref. [37]), in particular in frustrated systems where high entanglement is expected. Magnetization values are also known to be overstated by mean field expectation values.

Clearly, the calculation of more precise expectation values is necessary to properly evaluate the computed states. This would enable us to determine whether the states generated with the simple update procedure inadequately approximate the true ground

state, or if the discrepancies in the results originate from the mean field expectation values.

To this end we attempted to implement calculation of CTMRG expectation values on the iPESS states which turned out to be not easily possible, leaving us without clear results for the states obtained by simple update imaginary time evolution.

In the following section we will describe the challenges in calculating CTMRG expectation values for the obtained iPESS states.

3.2.3 Calculating CTMRG Expectation Values

Mean field expectation values are easy and numerically cheap to calculate, but they are a rough estimation, disregarding entanglement of the environment and can thus produce inaccurate results. The energies and magnetizations computed by this method on the states obtained by simple update with the iPESS ansatz give reason to conclude that, in this case, the mean field method is not sufficient to produce accurate results.

For this reason it is desirable to use a more precise method, utilizing the whole environment. To this end we chose to apply the CTMRG method, which was introduced in the previous chapter, to calculate expectation values for the obtained iPESS states.

Because the standard CTMRG method operates on square lattices, the iPESS network needs to be mapped to a square lattice by modifying the tensor network structure. The operations available to create such a mapping are:

- Coarse-graining: Contracting multiple tensors into one larger tensor, combining their physical degrees of freedom.
- Fine-graining [56]: Splitting a tensor into multiple parts using an isometry, each retaining part of the physical information, which when coarse-grained recover the original tensor.
- Rerouting contraction indices: Contracted indices between to tensors C and B can be routed over a mutually connected third tensor D by using a tensor product of D and an identity matrix (see Fig. 3.7).

The most straightforward mapping for the iPESS ansatz is coarse-graining a whole primitive unit cell of nine sites, obtaining a triangular tensor network structure which can be further transformed into a square PEPS by rerouting.

Starting from a floret pentagonal iPEPS or iPESS ansatz with bond dimension χ_B and physical dimension p the resulting square PEPS would have a new bond dimension $\chi_{\mathrm{B}_\mathrm{sq}} = \chi_\mathrm{B}^4$, and physical dimension $p_\mathrm{sq} = p^9$. A site tensor in such a mapping would thus be of size ${\chi_{\mathrm{B}_\mathrm{sq}}}^4 p_\mathrm{sq} = \chi_\mathrm{B}^{16} p^9$. These inflated dimensions resulting from the mapping

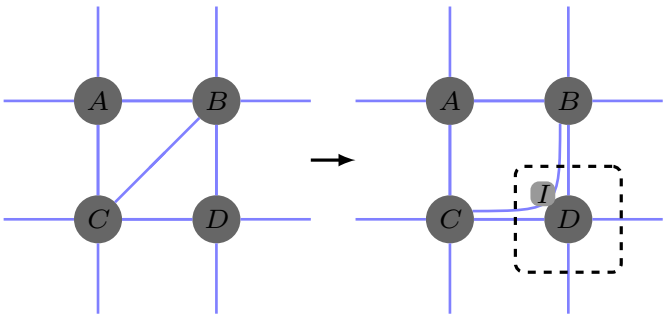

Figure 3.7: Illustration of rerouting a diagonal contraction over a mutually connected tensor.

to the square lattice make calculating CTMRG expectation values unfeasible for even moderate bond dimensions like $\chi_B = 5$ on current computing capabilities.

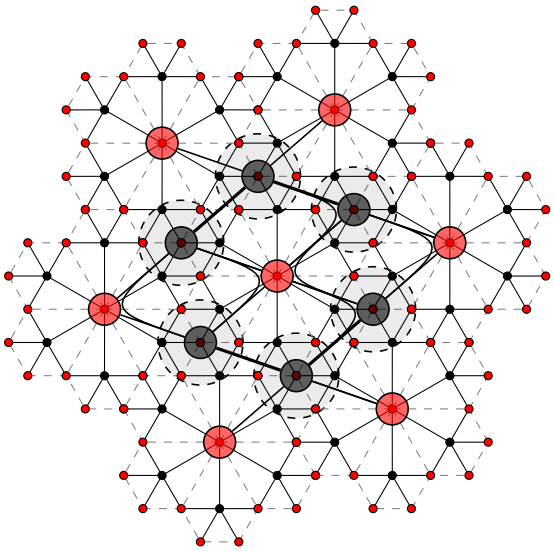

Figure 3.8: Mapping of the iPESS ansatz to a square lattice by coarse-graining four site and three simplex tensors and rerouting diagonal indices.

We considered alternative mappings (e.g. Fig. 3.8) with coarse-grainings smaller than the primitive unit cell. In this case the unit cell of the floret pentagonal lattice does not map to a unit cell of the square lattice. In the mapping depicted in Fig. 3.8 a single primitive unit cell of the floret pentagonal lattice maps to three tensors, but a three site unit cell is not possible in the square lattice. This shows that the mapping produces states which are not in general commensurate with the square lattice. Enlarging the unit cells in the mapping can mitigate this issue but further increases computational cost.

Calculating precise expectation values for the simulated iPESS states using CTMRG proved challenging, as the complex iPESS structure is not readily mapped to a square

lattice. Additionally, the calculated mean field energies suggest that the states obtained by simple update might not sufficiently approximate the ground state of the system. Consequently, we conclude that simple update on iPESS states is not an ideal method to investigate the problem of numerically examining the Heisenberg AFM on the floret pentagonal lattice.

Instead we turn to apply a different approach: Using CTMRG to calculate expectation values on a coarse-grained iPEPS state and finding ground states by variationally optimizing this state.

3.3 Investigation using Variational Optimization

Running simple update imaginary time evolution on iPESS states we encountered problems with calculating precise expectation values because we could not find an efficient mapping of the iPESS network to a square lattice topology.

Using CTMRG to calculate expectation values and variational optimization as described in Section 2.4.2, an iPEPS ansatz can be globally optimized to find ground state candidates, avoiding the need for iPESS states and allowing for a more precise computation of expectation values.

In this section we employ this approach to address the challenges of simulating the Heisenberg antiferromagnet on the floret pentagonal lattice. We begin by introducing the coarse-grained iPEPS ansatz, followed by a summary of the simulation procedure. Subsequently, we will present and analyze the results obtained from our investigation into the ground state energy and magnetization process of the model.

3.3.1 PEPS Ansatz

As the utilized CTMRG algorithm requires a square lattice iPEPS state, our ansatz has to conform to this requirement as well. Therefore, we chose an ansatz obtained by coarse-graining all nine sites in a primitive unit cell of the floret pentagonal lattice. This maps the floret pentagonal lattice to a triangular lattice, which can in turn be regarded as a square lattice with diagonal next-nearest neighbor interaction terms. In the resulting mapping (see Fig. 3.9), some interactions that were nearest neighbor interactions in the floret pentagonal lattice become next-nearest-neighbor terms. Namely, these are the interactions between sites 5 and 9 within one unit cell, and site 1 of the unit cell obtained by shifting along both lattice vector (marked blue in Fig. 3.9).

The choice of this mapping will in general have an influence on the resulting states and expectation values. Correlations within a coarse graining unit can be represented

exactly, while correlations between connected coarse tensors are limited by the bond dimension.

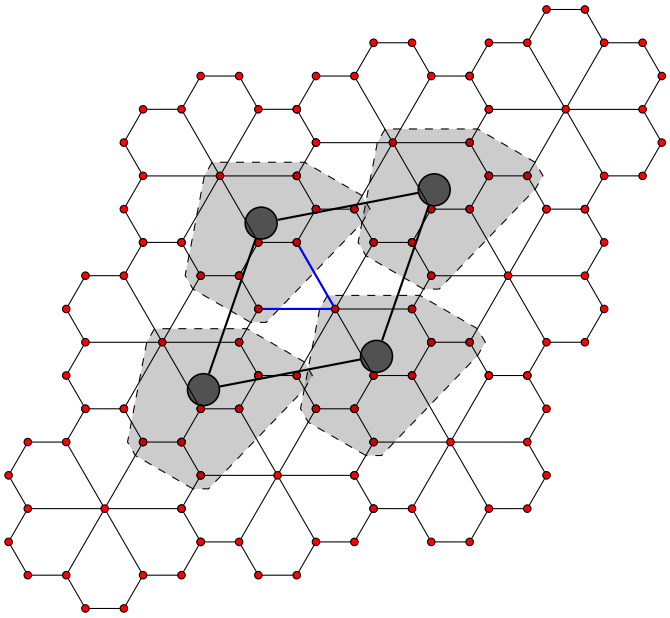

Figure 3.9: Coarse grained PEPS ansatz which was used for the variational optimization. In the ansatz one primitive unit cell of the lattice maps to one site tensor. Site tensors are connected to form a square lattice. Nearest neighbor interactions, which become next-nearest neighbor interactions in this mapping have been marked blue.

Due to coarse-graining the whole primitive unit cell, the individual PEPS tensors will have a physical dimension p^9. This poses a significant computational challenge, limiting the accessible bond dimensions in the variational update.

3.3.2 Simulation

To perform the variational optimization and calculation of CTMRG expectation values, the *variPEPS* [37] library was used. The chosen ansatz results in $2Np^9\chi_B^4$ real variational parameters for an N-site unit cell. The 2 stems from regarding real and imaginary part of the tensor entries as separate parameters in the context of optimization.

The variational state was initialized with random tensors. In the optimization process the update direction was determined using the conjugate gradient method and Wolfe conditions were used for the line search along the descent direction. Optimization was run until convergence which was determined by the norm of the gradient being below

a threshold. If convergence was not reached after a number of maximum steps the tensors were perturbed with random noise.

3.3.3 Results

Due to resource constraints while using the numerically intensive variational optimization on the coarse-grained ansatz, we restricted our simulations using this method to the case of equal interaction strengths $\eta = 1$, i.e. to the isotropic Heisenberg model.

Using the gradient based variational optimization method and our iPEPS ansatz (Fig. 3.9), we first ran simulations with bond dimension $\chi_B = 3$ to determine the most suitable choice of unit cell for the ground state at no external field h_z. To this end we probed the different unit cell structures $\mathcal{L}_9$, $\mathcal{L}_{18}$, $\mathcal{L}_{27}$, $\mathcal{L}_{36}$ and compared their optimized ground state energies (c.f. Table 3.4).

Unit Cell	$\mathcal{L}_9$	$\mathcal{L}_{18}$	$\mathcal{L}_{27}$	$\mathcal{L}_{36}$
$E_0(\chi_B = 3)$	-0.4623	-0.4801	-0.4773	-0.4805

Table 3.4: Variational energy per site for different unit cells of the iPEPS ansatz at bond dimension $\chi_B = 3$.

The ground state energies for the $\mathcal{L}_{18}$ and $\mathcal{L}_{36}$ patterns are close to equal and lesser than the results for $\mathcal{L}_9$ and $\mathcal{L}_{27}$. Further, investigating the nearest neighbor spin-spin correlations and z-axis magnetizations (as depicted for $\mathcal{L}_{18}$ in Fig. 3.12) of the $\mathcal{L}_{36}$ state reveal, that $c \sim b$ and $d \sim a$. Thus the $\mathcal{L}_{18}$ pattern is a likely candidate for the unit cell of the ground state at $h_z = 0$, although significantly larger unit cells have not been investigated. This result matches our preliminary analysis using the simple update method as discussed in Section 3.2.2.

Ground State without magnetic field

In order to determine the ground state energy of the Heisenberg antiferromagnet on the floret pentagonal lattice at $h_z = 0$ we ran a series of simulations for increasing bond dimension $\chi_B \in \{2, 3, 4, 5\}$ for the $\mathcal{L}_{18}$ unit cell. The results of this series are displayed in Table 3.5.

χ_B	2	3	4	5
E_0	-0.4683	-0.4801	-0.4884	-0.4905

Table 3.5: Per site energy E_0 of the isotropic Heisenberg AFM with no external magnetic field obtained for the $\mathcal{L}_{18}$ unit cell at different iPEPS bond dimensions χ_B.

To ensure accurate approximation of the expectation values, it is necessary to select a large enough environment bond dimension χ_E. We verified this to be the case by evaluating the state resulting of the simulation with a unit cell structure $\mathcal{L}_{18}$ and an iPEPS bond dimension $\chi_B = 5$, obtained by a variational optimization with environment bond dimension $\chi_E = 64$. For this fixed iPEPS state we probed the expectation values for different environment bond dimension $\chi_E \in \{1, ..., 64\}$. Convergence was observed around $\chi_E = 45$, as depicted in the log plot in Fig. 3.10. While the energy calculation stabilizes only at higher environment bond dimensions, the absolute difference in energy is already relatively low at 10^{-4} for $\chi_E = 4$. Given that the precision of the variational update and CTMRG does not exceed ten significant digits, the practical impact of choosing $\chi_E \geq 4$ to evaluate a fixed state is minimal.

Additionally we ran a series of variational update simulations with higher maximal bond dimensions $\chi_E \in \{68, 72, 76, 80\}$, starting from the $\mathcal{L}_{18}$ state obtained at $\chi_B = 5$ perturbed by random noise. The simulations in this series obtained the same ground state energy as the original state with $\chi_E = 64$. This indicates that the choice of maximal χ_E was sufficient to generate precise results for states with $\chi_B = 5$.

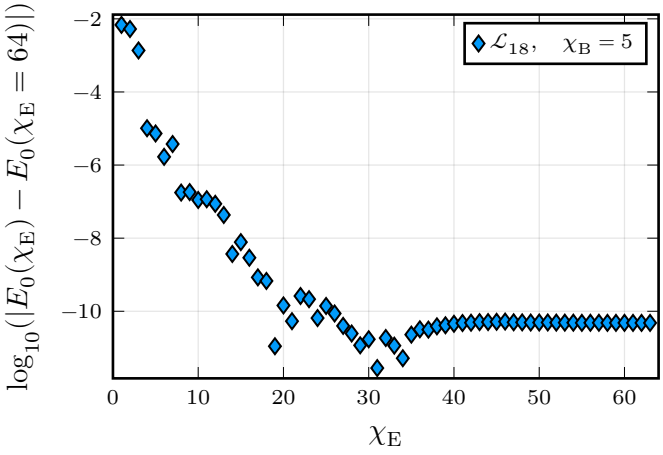

Figure 3.10: Convergence of the ground state energy with respect to the environment bond dimension χ_E. The input state has been obtained with a variational optimization of a $\mathcal{L}_{18}$ unit cell at $\chi_B = 5$ and $\chi_E = 64$.

Having reached convergence in χ_E in the simulations, the energies in Table 3.5 are variational in that they serve as a valid upper bound for the ground state energy of our model on the floret pentagonal lattice.

The finite bond dimension χ_B in our simulations imposes a an effective length scale, limiting the possible range of spin correlations. As explained in Section 2.5, this length scale can be measured by the correlation length ξ. To give an estimate for the physical ground state energy in the limit of $\chi_B \to \infty$, where the length scale is unrestricted, we extrapolate the energies obtained for different χ_B to the limit $\xi \to \infty$.

For this we applied a linear regression to retrieve the relation expected between ξ^{-3} and $E_0(\xi)$ [52, 50] (c.f. Fig. 3.11). The regression leads to a relation

$$\begin{aligned} E_0(\xi) &= \frac{a}{\xi^3} - E_0^{\xi=\infty}, \text{ with} \\ a &= (9.9 \pm 0.7) \cdot 10^{-5} \\ E_0^{\xi=\infty} &= -0.501 \pm 0.002. \end{aligned} \tag{3.7}$$

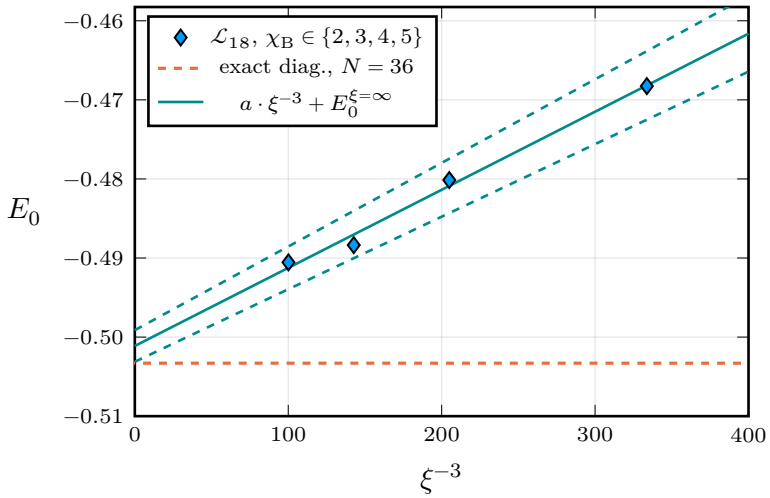

Figure 3.11: Energies of $\mathcal{L}_{18}$ unit cell simulations from $\chi_B = 2$ to $\chi_B = 5$ against the third power of the inverse correlation length. A linear fit of the energies yields a relation of $a = (9.9 \pm 0.7) \cdot 10^{-5}$ and $E_0^{\xi=\infty} = -0.501 \pm 0.002$. The horizontal line marks the ground state energy reported by Furuchi et al. [20] for the largest of the finite clusters (36 sites).

This extrapolated value at infinite correlation length gives an estimate for the energy at infinite bond dimension $E_0(\chi_B \to \infty)$.

To further characterize the ground state of the floret pentagonal Heisenberg antiferromagnet, we investigated the spatial pattern of spin-spin correlations $\langle \mathbf{S}_i \cdot \mathbf{S}_j \rangle$ and local z-axis magnetizations $\langle S_i^z \rangle$ as seen in Fig. 3.12.

Noticeably, the nearest neighbor interactions with the smallest negative contribution to the energy are the two $A \to B$ interactions at angles 120° and 300°. This might be an artifact of choosing a coarse graining ansatz that is missing a direct contraction along this direction, similar to the square lattice with diagonal interactions. In order to determine if the ansatz merely determines the direction of this weaker contribution or if this is a general property of the ground state, simulations with different coarse graining structure are required.

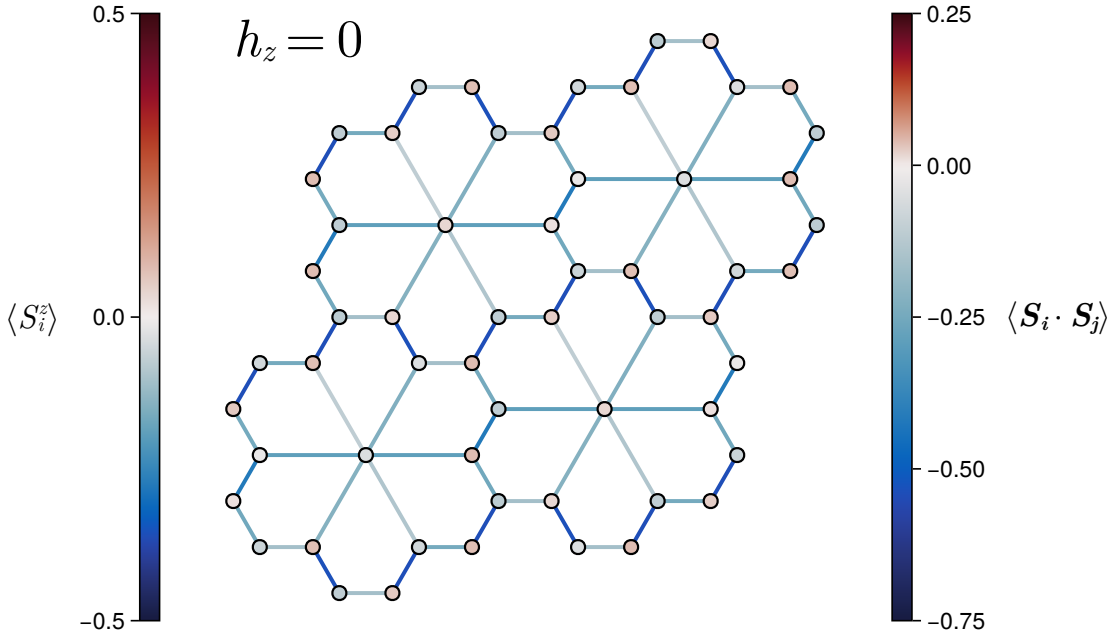

Figure 3.12: Expectation values of the z-component of the spin and spin-spin correlations for the $\mathcal{L}_{18}$ unit cell at $h_z = 0$ and $\chi_B = 5$. The lattice symmetry appears to be broken such that a $\mathcal{L}_9$ unit cell would not suffice to represent this state.

Magnetization Process

As a geometrically frustrated spin system the magnetization process of the floret pentagonal lattice is of special interest. Interactions of quantum fluctuations with classical degenerate ground state can produce features unique to such systems like magnetization plateaus and jumps.

To investigate this process we run a series of simulations with varying external magnetic field strengths from $h_z = 0$ to $h_z = 4$ in steps of 0.1. Because the unit cell for those ground states is not necessarily the same as for $h_z = 0$, these simulations were run for unit cells $\mathcal{L}_{18}$, $\mathcal{L}_{27}$ and $\mathcal{L}_{36}$ at bond dimension $\chi_\mathrm{B} = 3$.

Fig. 3.13 shows a plot of the average magnetization along the axis of the external field divided by the maximal magnetization value $\overline{m_z}/m_\mathrm{s}$ dependent on h_z. Apart from data points close to $h_z = 0$ the values of $\overline{m_z}/m_\mathrm{s}$ closely coincide for all chosen unit cells, suggesting a simple $\mathcal{L}_9$ unit cell as a suitable structure for values of $h_z \gg 0$. We observe two magnetization plateaus at $\overline{m_z}/m_\mathrm{s} = \frac{3}{9}$ and $\overline{m_z}/m_\mathrm{s} = \frac{7}{9}$, the first one at $0.5 \leq h_z \leq 1.5$ and the other one at $2.1 \leq h_z \leq 3.6$. Plateaus at the same $\overline{m_z}/m_\mathrm{s}$ and h_z ranges have been reported in Ref. [20].

In the $\frac{3}{9}$-plateau spins on type B sites are mostly aligned with the magnetic field and type A and C sites are mostly aligned against it (c.f. Fig. 3.14). At even higher field strength in the $\frac{7}{9}$-plateau the B and C sites are almost fully aligned with the external field, while the type A sites are still slightly anti-aligned.

Furthermore, Furuchi et al. found that there is a plateau at $\overline{m_z}/m_\mathrm{s} = \frac{1}{9}$ within a narrow range of h_z, as well as a magnetization jump around $\overline{m_z}/m_\mathrm{s} = \frac{11}{18}$. Because of the small range in h_z of the plateau, it would be necessary for us to collect additional data points around $0 \leq h_z \leq \frac{1}{2}$ to confirm its existence. Furthermore, the significant gradient observed around $\overline{m_z}/m_\mathrm{s} = \frac{11}{18}$ suggests the possibility of a discontinuity. Therefore, it is required to collect more data points around $h_z = 2$ to accurately understand the behavior in this region and confirm the presence of a jump in magnetization.

The z-magnetization curves for the different unit cells are congruent for large parts of the h_z range, particularly in the range of the two plateaus. This indicates that the ground states in these parts of the curve show a $\mathcal{L}_9$ unit cell structure made up of a single primitive unit cell. This is further supported by the structure of z-axis spin magnetization $\langle S_i^z \rangle$ and nearest neighbor spin correlations $\langle \mathbf{S}_i \cdot \mathbf{S}_j \rangle$ displayed in Fig. 3.14 for two states belonging to either plateau.

The Oshikawa-Yamanaka-Affleck (OYA) criterion [57] restricts magnetization plateaus to average per site magnetizations $\overline{m}_z$ where

$$p = n\,(S - \overline{m}_z) \tag{3.8}$$

is an integer value. Here S refers to the spin value of a single site.

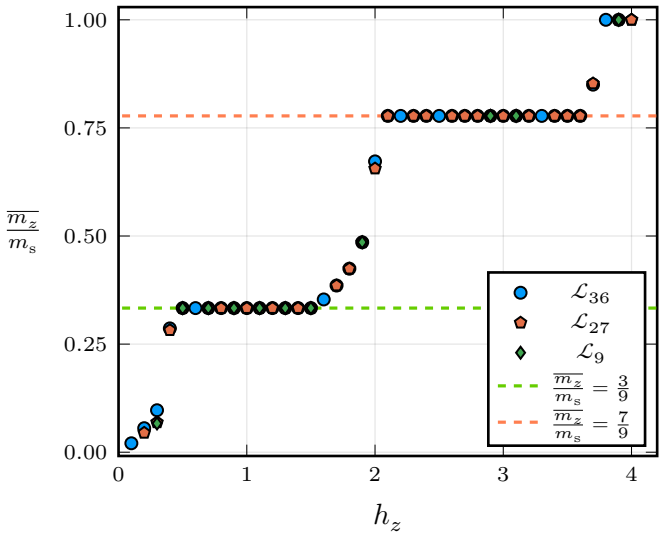

(a)

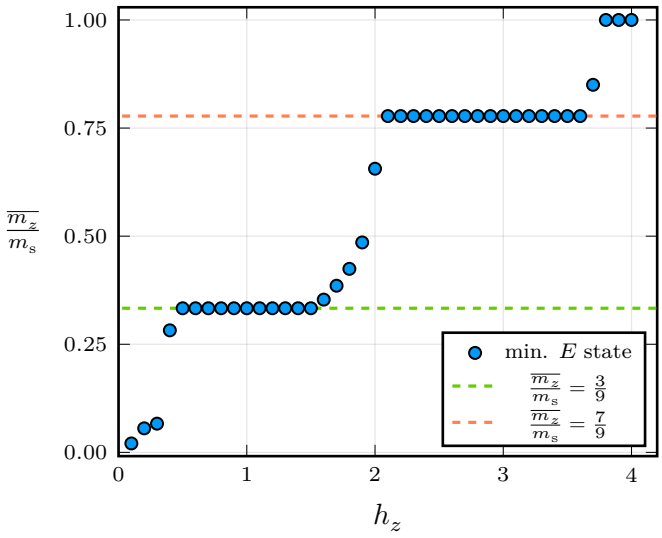

(b)

Figure 3.13: Magnetization process dependent on external field strength h_z. $\overline{m_z}/m_s$ is average z-axis magnetization $\overline{m_z}$ divided by the saturation value $m_s = \frac{1}{2}$.
(a) shows the magnetizations curves obtained in simulations with unit cells $\mathcal{L}_{18}$, $\mathcal{L}_{27}$ and $\mathcal{L}_{36}$.
(b) shows the curve for the states with the lowest energy for the respective h_z.
Magnetization plateaus at $\overline{m_z}/m_s = \frac{3}{9}$ and $\overline{m_z}/m_s = \frac{7}{9}$ have been marked with horizontal lines.All values were obtained at $\chi_B = 3$.

While initially formulated for non-frustrated 1D systems the OYA criterion has since been extended to anti-ferromagnetic systems in arbitrary dimensions [58] and recently to frustrated anti-ferromagnetic systems [59].

In lattices with small basis this criterion necessitates an increased unit cell in the plateau regime, introducing a phase transition. In the case of the floret pentagonal lattice the number of sites in a unit cell n is already relatively large for the primitive unit cell, allowing for plateaus at $\overline{m_z}/m_\mathrm{s} \in \{\frac{1}{9}, \frac{3}{9}, \frac{5}{9}, \frac{7}{9}\}$ without requiring a larger unit cell. Still, we observe a phase transition from the $\mathcal{L}_{18}$ structure of the ground state at zero magnetic field to the primitive unit cell in the plateaus.

The general configurations of spins on the plateaus (c.f. Fig. 3.14) bear resemblance to the ground states of the corresponding Ising and classical Heisenberg models at certain h_z, although both classical models show stronger alignment with the external field. This indicates that the quantum ground states might not have a correspondence in the classical ground space manifold. Furthermore, is noticeable that the observed plateaus seem to start around h_z ranges where the magnetization curve of the classical model (c.f. Ref. [20, Fig. 3]) has maximum curvature.

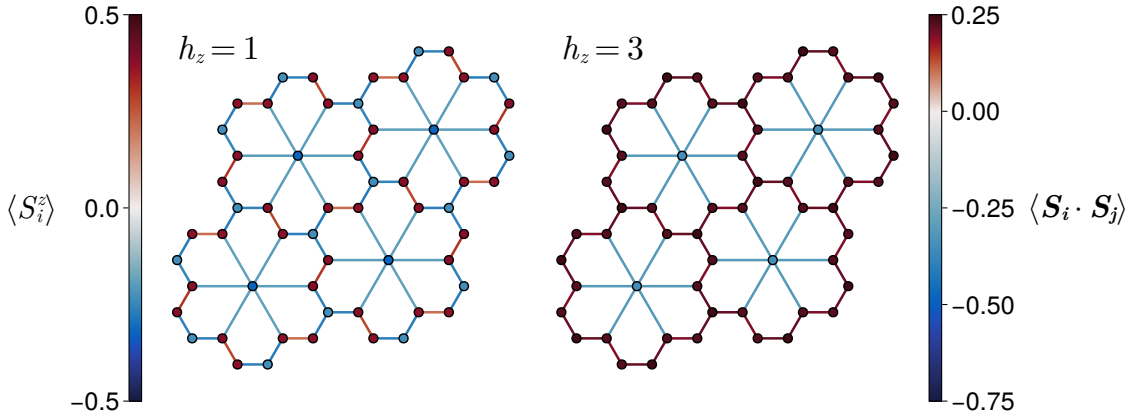

Figure 3.14: Expectation values of the z-component of the spin and spin-spin correlations for the $\mathcal{L}_{36}$ unit cell at different external field strengths h_z. $h_z = 1$ is displayed as a representative of the $\overline{m_z}/m_\mathrm{s} = \frac{3}{9}$ plateau and $h_z = 3$ for the plateau at $\overline{m_z}/m_\mathrm{s} = \frac{7}{9}$.

4 Conclusion

In this thesis we investigated frustrated quantum magnetism on pentagon based lattices using tensor network methods in two spatial dimensions at the example of the floret pentagonal lattice. Given its geometric structure, this lattice has the potential to host interesting quantum many-body phases while being challenging to deal with from an numerical perspective. With a focus on the (anisotropic) Heisenberg model, this constitutes the first numerical study of the model by means of infinite 2D tensor network methods.

For the initial investigation of the floret pentagonal Heisenberg model we chose two different tensor network structures, namely the infinite PEPS and PESS methods. For the optimization of the ground state wave function on these states we employed the common simple update technique, which was unsuccessful on the iPEPS ansatz of the floret pentagonal lattice, but led to feasible quantum states for the dual iPESS approach.

To obtain preliminary approximate results for the optimized quantum states we calculated expectation values using the mean field method, but the calculated energies were far from the ones reported in the finite cluster study and the predicted magnetization values were untypical for antiferromagnetic systems.

More precise calculations of expectation values using CTMRG proved to be challenging due to the high coordination numbers of the iPESS ansatz and the resulting difficulties in mapping it to a square lattice, which is required for the application of CTMRG. A mapping applying a coarse graining to a whole unit cell was possible but was considered numerically unfeasible for CTMRG because of the large dimension of resulting tensors. Other mappings were not commensurate with the square lattice.

After the examination of the model using simple update was inconclusive, as the method proved not suitable for obtaining accurate results, we turned to a different approach: We coarse grained all nine sites of the primitive unit cell and linked the coarse-grained site tensors in the directions of the lattice vectors, obtaining a square lattice iPEPS with diagonal next-nearest neighbor interactions. Using this ansatz we obtained ground states using variational update and calculated expectation values on these states with CTMRG. As this method incurred significantly higher numerical cost, we limited the simulations to the case of isotropic spin interactions $\eta = 1$.

To identify the translation symmetry of the ground state we compared energy values and spin structure for different unit cells at $\chi_\mathrm{B} = 3$ and identified the $\mathcal{L}_{18}$ structure as a likely candidate for the unit cell of the ground state at $h_z = 0$.

An upper bound for the per-site ground state energy at no external field was calculated at bond dimension $\chi_\mathrm{B} = 5$ to be $E_0 = -0.4905$. To give an estimate for the ground state energy in the limit of infinite bond dimension we extrapolated the energy for states of different bond dimensions $\chi_\mathrm{B} \in \{2, 3, 4, 5\}$ in their correlation length ξ and arrived at an estimate of $E_0 = -0.501 \pm 0.002$ for the per site energy. This estimate for the physical energy of the ground state at h_z is close to the one reported by Furuchi et al. for the largest cluster in their investigation $E_0^{N=36} = -0.503$.

Examination of the properties of the model at varying magnetic field h_z showed two magnetization plateaus at $\overline{m_z}/m_\mathrm{s} = \frac{3}{9}$ and $\overline{m_z}/m_\mathrm{s} = \frac{7}{9}$. In contrast to the ground state at $h_z = 0$ the ground states on these plateaus conformed to translation symmetry of the floret pentagonal lattice.

5 Outlook

In this thesis we examined the Heisenberg antiferromagnet on the floret pentagonal lattice as a model of frustrated magnetism on pentagonal lattices. While important properties like ground state energies and the magnetization process have been surveyed, there are still many avenues to further study this model.

Upon examination of the obtained ground state for $h_z = 0$, it was observed that the weakest negative spin-spin interactions occurred along diagonally adjacent site tensors, which were not directly connected in the iPEPS ansatz. These weaker contributions could be an artifact of the chosen tensor network representation. Simulations using different coarse-graining ansatzes could elucidate if the ansatz caused this or merely determined the direction of these weaker interactions.

While we found magnetization plateaus at $\overline{m_z}/m_\mathrm{s} = \frac{3}{9}$ and $\overline{m_z}/m_\mathrm{s} = \frac{7}{9}$, another magnetization plateau at $\overline{m_z}/m_\mathrm{s} = \frac{1}{9}$ and a magnetization jump at around $\overline{m_z}/m_\mathrm{s} = \frac{11}{18}$ were reported by Furuchi et al. As it is not clear that those features also appear in the thermodynamic limit, it would be interesting to perform further tensor network simulations with a higher density of magnetic field values in the respective ranges to probe it.

In consequence of the high numerical cost of the variational update algorithm and limited HPC resources the results of this thesis were limited to the case of isotropic interaction $\eta = 1$. Further inquiry may be directed into the properties of the system at different interaction ratios η. For $\eta > 1.5$ Ref. [21] reports an additional magnetization plateau at $\overline{m_z}/m_\mathrm{s} = \frac{5}{9}$, which would be instructive to characterize.

The computational cost of calculating CTMRG expectation values and variational update simulations grows with unit cell size and is already quite significant at small sizes. This restricted us to exploring small unit cell sizes of up to 36 sites for the floret pentagonal lattice and leaves open the question if a larger unit cell might be better suited to represent the ground states of the model. Recently, a method has been proposed using only the primitive unit cell tensors and modeling bigger unit cells by transforming adjacent primitive unit cells with a periodic unitary [60]. In this way a suitable unit cell can be automatically found during a variational optimization of the lattice, but this development was too recent to be still considered in this work. Although the method is restricted to $SU(2)$-symmetric Hamiltonians and therefore can not be applied for $h_z \neq 0$, only having to optimize a single primitive unit could

lead to feasibility of simulating higher bond dimensions. Additionally the "learning" of the unit cell by variational optimization would enable to explore larger unit cell sizes, possibly finding a symmetry better suited to represent the ground state of the model.

Finally, frustrated magnetism in other pentagonal lattices could investigated. A particularly interesting candidate in this regard is the cairo pentagonal lattice, as two materials with antiferromagnetic cairo pentagonal layers ($Bi_2Fe_4O_9$ [61] and $Bi_4Fe_5O_{13}F$ [62]) have been found. The Heisenberg antiferromagnetic model on cairo pentagonal lattices has been studied using spin wave theory [63] and exact diagonalization techniques [64].

References

[1] Loris Bennett, Bernd Melchers, and Boris Proppe. *Curta: A General-purpose High-Performance Computer at ZEDAT, Freie Universität Berlin*. 2020. DOI: 10.17169/REFUBIUM-26754. URL: https://refubium.fu-berlin.de/handle/fub188/26993.

[2] M. J. Harris et al. "Geometrical Frustration in the Ferromagnetic Pyrochlore $Ho_2Ti_2O_7$". In: *Physical Review Letters* 79.13 (1997), pp. 2554–2557. DOI: 10.1103/physrevlett.79.2554. URL: http://dx.doi.org/10.1103/PhysRevLett.79.2554.

[3] C. Castelnovo, R. Moessner, and S. L. Sondhi. "Magnetic Monopoles in Spin Ice". In: *Nature* 451.7174 (2008), pp. 42–45. DOI: 10.1038/nature06433. URL: http://dx.doi.org/10.1038/nature06433.

[4] P.W. Anderson. "Resonating Valence Bonds: a New Kind of Insulator?" In: *Materials Research Bulletin* 8.2 (1973), pp. 153–160. DOI: 10.1016/0025-5408(73)90167-0. URL: http://dx.doi.org/10.1016/0025-5408(73)90167-0.

[5] P. W. Anderson. "The Resonating Valence Bond State in La_2CuO_4 and Superconductivity". In: *Science* 235.4793 (1987), pp. 1196–1198. DOI: 10.1126/science.235.4793.1196. URL: http://dx.doi.org/10.1126/science.235.4793.1196.

[6] Steven A. Kivelson, Daniel S. Rokhsar, and James P. Sethna. "Topology of the Resonating Valence-Bond State: Solitons and High-T_c superconductivity". In: *Physical Review B* 35.16 (1987), pp. 8865–8868. DOI: 10.1103/physrevb.35.8865. URL: http://dx.doi.org/10.1103/PhysRevB.35.8865.

[7] E. F. Shender and P. C. W. Holdsworth. "Order by Disorder and Topology in Frustrated Magnetic Systems". In: *Institute for Nonlinear Science*. Springer US, 1996, pp. 259–279. ISBN: 9781461239925. DOI: 10.1007/978-1-4612-3992-5_16. URL: http://dx.doi.org/10.1007/978-1-4612-3992-5_16.

[8] J. Eisert, M. Cramer, and M. B. Plenio. "*Colloquium*: Area Laws for the Entanglement Entropy". In: *Reviews of Modern Physics* 82.1 (2010), pp. 277–306. DOI: 10.1103/revmodphys.82.277. URL: http://dx.doi.org/10.1103/RevModPhys.82.277.

[9] Stellan Östlund and Stefan Rommer. "Thermodynamic Limit of Density Matrix Renormalization". In: *Physical Review Letters* 75.19 (1995), pp. 3537–3540. DOI: 10.1103/physrevlett.75.3537. URL: http://dx.doi.org/10.1103/PhysRevLett.75.3537.

[10] Steven R. White. "Density Matrix Formulation for Quantum Renormalization Groups". In: *Physical Review Letters* 69.19 (1992), pp. 2863–2866. DOI: 10.1103/physrevlett.69.2863. URL: http://dx.doi.org/10.1103/PhysRevLett.69.2863.

[11] F. Verstraete and J. I. Cirac. *Renormalization algorithms for Quantum-Many Body Systems in two and higher dimensions*. 2004. DOI: 10.48550/ARXIV.COND-MAT/0407066. URL: https://arxiv.org/abs/cond-mat/0407066.

[12] J. Jordan et al. "Classical Simulation of Infinite-Size Quantum Lattice Systems in Two Spatial Dimensions". In: *Physical Review Letters* 101.25 (Dec. 2008). ISSN: 1079-7114. DOI: 10.1103/physrevlett.101.250602. URL: http://dx.doi.org/10.1103/physrevlett.101.250602.

[13] Michael Levin and Cody P. Nave. "Tensor Renormalization Group Approach to Two-Dimensional Classical Lattice Models". In: *Physical Review Letters* 99.12 (Sept. 2007). ISSN: 1079-7114. DOI: 10.1103/physrevlett.99.120601. URL: http://dx.doi.org/10.1103/physrevlett.99.120601.

[14] Qian Li et al. "Magnetization of the Spin-$\frac{1}{2}$ Heisenberg Antiferromagnet on the Triangular Lattice". In: *Physical Review B* 105.18 (2022). ISSN: 2469-9969. DOI: 10.1103/physrevb.105.184418. URL: http://dx.doi.org/10.1103/PhysRevB.105.184418.

[15] Meng Zhang et al. "Projected Entangled Pair States Study of Anisotropic-Exchange Magnets on the Triangular Lattice". In: *Physical Review B* 105.2 (2022), p. 024411. DOI: 10.1103/physrevb.105.024411. URL: http://dx.doi.org/10.1103/PhysRevB.105.024411.

[16] Chen Zeng and Veit Elser. "Numerical Studies of Antiferromagnetism on a Kagomé Net". In: *Physical Review B* 42.13 (1990), pp. 8436–8444. DOI: 10.1103/physrevb.42.8436. URL: http://dx.doi.org/10.1103/PhysRevB.42.8436.

[17] Z. Y. Xie et al. "Tensor Renormalization of Quantum Many-Body Systems Using Projected Entangled Simplex States". In: *Physical Review X* 4.1 (Feb. 2014). ISSN: 2160-3308. DOI: 10.1103/physrevx.4.011025. URL: http://dx.doi.org/10.1103/physrevx.4.011025.

[18] Augustine Kshetrimayum et al. "Spin-$\frac{1}{2}$ kagome XXZ model in a field: Competition between lattice nematic and solid orders". In: *Physical Review B* 94.23 (Dec. 2016). ISSN: 2469-9969. DOI: 10.1103/physrevb.94.235146. URL: http://dx.doi.org/10.1103/PhysRevB.94.235146.

[19] Philipp Schmoll and Román Orús. "Benchmarking global $SU(2)$ symmetry in two-dimensional tensor network algorithms". In: *Physical Review B* 102.24 (Dec. 2020). ISSN: 2469-9969. DOI: 10.1103/physrevb.102.241101. URL: http://dx.doi.org/10.1103/physrevb.102.241101.

[20] Rito Furuchi et al. "Magnetization process of the S = 1/2 Heisenberg antiferromagnet on the floret pentagonal lattice". In: *Journal of Physics Communications* 5.12 (Dec. 2021), p. 125008. ISSN: 2399-6528. DOI: 10.1088/2399-6528/ac3f7a. URL: http://dx.doi.org/10.1088/2399-6528/ac3f7a.

[21] Rito Furuchi, Hiroki Nakano, and Tôru Sakai. "Numerical Study of $S = 1/2$ Heisenberg Antiferromagnet on the Floret Pentagonal Lattice". In: *Proceedings of the 29th International Conference on Low Temperature Physics (LT29)*. Journal of the Physical Society of Japan, May 2023. DOI: 10.7566/jpscp.38.011167. URL: http://dx.doi.org/10.7566/jpscp.38.011167.

[22] Norbert Schuch et al. "Resonating valence bond states in the PEPS formalism". In: *Physical Review B* 86.11 (Sept. 2012). ISSN: 1550-235X. DOI: 10.1103/physrevb.86.115108. URL: http://dx.doi.org/10.1103/physrevb.86.115108.

[23] Yimin Ge and Jens Eisert. "Area laws and efficient descriptions of quantum many-body states". In: *New Journal of Physics* 18.8 (Aug. 2016), p. 083026. ISSN: 1367-2630. DOI: 10.1088/1367-2630/18/8/083026. URL: http://dx.doi.org/10.1088/1367-2630/18/8/083026.

[24] E. Y. Loh et al. "Sign Problem in the Numerical Simulation of Many-Electron Systems". In: *Physical Review B* 41.13 (1990), pp. 9301–9307. DOI: 10.1103/physrevb.41.9301. URL: http://dx.doi.org/10.1103/PhysRevB.41.9301.

[25] U. Schollwöck. "The Density-Matrix Renormalization Group". In: *Reviews of Modern Physics* 77.1 (2005), pp. 259–315. DOI: 10.1103/revmodphys.77.259. URL: http://dx.doi.org/10.1103/RevModPhys.77.259.

[26] Román Orús. "A practical introduction to tensor networks: Matrix product states and projected entangled pair states". In: *Annals of Physics* 349 (Oct. 2014), pp. 117–158. ISSN: 0003-4916. DOI: 10.1016/j.aop.2014.06.013. URL: http://dx.doi.org/10.1016/j.aop.2014.06.013.

[27] Arturo Acuaviva et al. "The minimal canonical form of a tensor network". In: (2022). DOI: 10.48550/ARXIV.2209.14358. URL: https://arxiv.org/abs/2209.14358.

[28] Henning Kalis et al. "Fate of the cluster state on the square lattice in a magnetic field". In: *Physical Review A* 86.2 (Aug. 2012). ISSN: 1094-1622. DOI: 10.1103/physreva.86.022317. URL: http://dx.doi.org/10.1103/physreva.86.022317.

[29] Norbert Schuch et al. “Computational Complexity of Projected Entangled Pair States”. In: *Physical Review Letters* 98.14 (Apr. 2007). ISSN: 1079-7114. DOI: 10.1103/physrevlett.98.140506. URL: http://dx.doi.org/10.1103/physrevlett.98.140506.

[30] M. Schwarz, O. Buerschaper, and J. Eisert. “Approximating local observables on projected entangled pair states”. In: *Physical Review A* 95.6 (June 2017). ISSN: 2469-9934. DOI: 10.1103/physreva.95.060102. URL: http://dx.doi.org/10.1103/physreva.95.060102.

[31] F. Verstraete et al. “Criticality, the Area Law, and the Computational Power of Projected Entangled Pair States”. In: *Physical Review Letters* 96.22 (June 2006). ISSN: 1079-7114. DOI: 10.1103/physrevlett.96.220601. URL: http://dx.doi.org/10.1103/physrevlett.96.220601.

[32] Román Orús and Guifré Vidal. “Simulation of two-dimensional quantum systems on an infinite lattice revisited: Corner transfer matrix for tensor contraction”. In: *Physical Review B* 80.9 (Sept. 2009). ISSN: 1550-235X. DOI: 10.1103/physrevb.80.094403. URL: http://dx.doi.org/10.1103/physrevb.80.094403.

[33] Guifré Vidal. “Efficient Classical Simulation of Slightly Entangled Quantum Computations”. In: *Physical Review Letters* 91.14 (Oct. 2003). ISSN: 1079-7114. DOI: 10.1103/physrevlett.91.147902. URL: http://dx.doi.org/10.1103/physrevlett.91.147902.

[34] Saeed S. Jahromi and Román Orús. “Universal tensor-network algorithm for any infinite lattice”. In: *Physical Review B* 99.19 (May 2019). ISSN: 2469-9969. DOI: 10.1103/physrevb.99.195105. URL: http://dx.doi.org/10.1103/physrevb.99.195105.

[35] I. V. Lukin and A. G. Sotnikov. “Variational optimization of tensor-network states with the honeycomb-lattice corner transfer matrix”. In: *Physical Review B* 107.5 (Feb. 2023). ISSN: 2469-9969. DOI: 10.1103/physrevb.107.054424. URL: http://dx.doi.org/10.1103/physrevb.107.054424.

[36] I. V. Lukin and A. G. Sotnikov. *Corner transfer matrix renormalization group approach in the zoo of Archimedean lattices*. 2024. DOI: 10.48550/ARXIV.2401.07274. URL: https://arxiv.org/abs/2401.07274.

[37] Jan Naumann et al. *variPEPS – a versatile tensor network library for variational ground state simulations in two spatial dimensions*. 2023. DOI: 10.48550/ARXIV.2308.12358. URL: https://arxiv.org/abs/2308.12358.

[38] Philippe Corboz, T. M. Rice, and Matthias Troyer. “Competing States in the t-J Model: Uniform d-Wave State versus Stripe State”. In: *Physical Review Letters* 113.4 (July 2014). ISSN: 1079-7114. DOI: 10.1103/physrevlett.113.046402. URL: http://dx.doi.org/10.1103/physrevlett.113.046402.

[39] V. Zauner-Stauber et al. “Variational optimization algorithms for uniform matrix product states”. In: *Physical Review B* 97.4 (Jan. 2018). ISSN: 2469-9969. DOI: 10.1103/physrevb.97.045145. URL: http://dx.doi.org/10.1103/physrevb.97.045145.

[40] Wangwei Lan and Glen Evenbly. *Reduced Contraction Costs of Corner-Transfer Methods for PEPS*. 2023. DOI: 10.48550/ARXIV.2306.08212. URL: https://arxiv.org/abs/2306.08212.

[41] H. C. Jiang, Z. Y. Weng, and T. Xiang. “Accurate Determination of Tensor Network State of Quantum Lattice Models in Two Dimensions”. In: *Physical Review Letters* 101.9 (Aug. 2008). ISSN: 1079-7114. DOI: 10.1103/physrevlett.101.090603. URL: http://dx.doi.org/10.1103/physrevlett.101.090603.

[42] G. Vidal. “Classical Simulation of Infinite-Size Quantum Lattice Systems in One Spatial Dimension”. In: *Physical Review Letters* 98.7 (Feb. 2007). ISSN: 1079-7114. DOI: 10.1103/physrevlett.98.070201. URL: http://dx.doi.org/10.1103/physrevlett.98.070201.

[43] Masuo Suzuki. “Fractal decomposition of exponential operators with applications to many-body theories and Monte Carlo simulations”. In: *Physics Letters A* 146.6 (June 1990), pp. 319–323. ISSN: 0375-9601. DOI: 10.1016/0375-9601(90)90962-n. URL: http://dx.doi.org/10.1016/0375-9601(90)90962-n.

[44] Guifré Vidal. “Efficient Simulation of One-Dimensional Quantum Many-Body Systems”. In: *Physical Review Letters* 93.4 (July 2004). ISSN: 1079-7114. DOI: 10.1103/physrevlett.93.040502. URL: http://dx.doi.org/10.1103/physrevlett.93.040502.

[45] Ho N. Phien et al. “Infinite projected entangled pair states algorithm improved: Fast full update and gauge fixing”. In: *Physical Review B* 92.3 (July 2015). ISSN: 1550-235X. DOI: 10.1103/physrevb.92.035142. URL: http://dx.doi.org/10.1103/physrevb.92.035142.

[46] Philippe Corboz. “Variational optimization with infinite projected entangled-pair states”. In: *Physical Review B* 94.3 (July 2016). ISSN: 2469-9969. DOI: 10.1103/physrevb.94.035133. URL: http://dx.doi.org/10.1103/physrevb.94.035133.

[47] Lieven De Lathauwer, Bart De Moor, and Joos Vandewalle. “A Multilinear Singular Value Decomposition”. In: *SIAM Journal on Matrix Analysis and Applications* 21.4 (2000), pp. 1253–1278. DOI: 10.1137/s0895479896305696. URL: http://dx.doi.org/10.1137/S0895479896305696.

[48] Laurens Vanderstraeten et al. “Gradient methods for variational optimization of projected entangled-pair states”. In: *Physical Review B* 94.15 (Oct. 2016). ISSN: 2469-9969. DOI: 10.1103/physrevb.94.155123. URL: http://dx.doi.org/10.1103/physrevb.94.155123.

[49] Hai-Jun Liao et al. “Differentiable Programming Tensor Networks”. In: *Physical Review X* 9.3 (Sept. 2019). ISSN: 2160-3308. DOI: 10.1103/physrevx.9.031041. URL: http://dx.doi.org/10.1103/physrevx.9.031041.

[50] Bram Vanhecke et al. “Scaling Hypothesis for Projected Entangled-Pair States”. In: *Physical Review Letters* 129.20 (Nov. 2022). ISSN: 1079-7114. DOI: 10.1103/physrevlett.129.200601. URL: http://dx.doi.org/10.1103/physrevlett.129.200601.

[51] Marek M. Rams, Piotr Czarnik, and Lukasz Cincio. “Precise Extrapolation of the Correlation Function Asymptotics in Uniform Tensor Network States with Application to the Bose-Hubbard and XXZ Models”. In: *Physical Review X* 8.4 (Nov. 2018). ISSN: 2160-3308. DOI: 10.1103/physrevx.8.041033. URL: http://dx.doi.org/10.1103/physrevx.8.041033.

[52] Michael Rader and Andreas M. Läuchli. “Finite Correlation Length Scaling in Lorentz-Invariant Gapless iPEPS Wave Functions”. In: *Physical Review X* 8.3 (July 2018). ISSN: 2160-3308. DOI: 10.1103/physrevx.8.031030. URL: http://dx.doi.org/10.1103/physrevx.8.031030.

[53] *Quantum Magnetism*. Lecture Notes in Physics. Springer Berlin Heidelberg, 2004. ISBN: 9783540400660. DOI: 10.1007/b96825. URL: http://dx.doi.org/10.1007/b96825.

[54] Finn Krein. *Simple Update*. Version 0.1.0. Mar. 2024. DOI: 10.5281/zenodo.10789747. URL: https://doi.org/10.5281/zenodo.10789747.

[55] Jutho et al. *Jutho/TensorOperations.jl: v3.2.5*. Version v3.2.5. Apr. 2023. DOI: 10.5281/zenodo.7844764. URL: https://doi.org/10.5281/zenodo.7844764.

[56] Philipp Schmoll et al. “Fine Grained Tensor Network Methods”. In: *Physical Review Letters* 124.20 (May 2020). ISSN: 1079-7114. DOI: 10.1103/physrevlett.124.200603. URL: http://dx.doi.org/10.1103/physrevlett.124.200603.

[57] Masaki Oshikawa, Masanori Yamanaka, and Ian Affleck. “Magnetization Plateaus in Spin Chains: ”Haldane Gap” for Half-Integer Spins”. In: *Physical Review Letters* 78.10 (1997), pp. 1984–1987. DOI: 10.1103/physrevlett.78.1984. URL: http://dx.doi.org/10.1103/PhysRevLett.78.1984.

[58] Akihiro Tanaka, Keisuke Totsuka, and Xiao Hu. “Geometric phases and the magnetization process in quantum antiferromagnets”. In: *Physical Review B* 79.6 (Feb. 2009). ISSN: 1550-235X. DOI: 10.1103/physrevb.79.064412. URL: http://dx.doi.org/10.1103/physrevb.79.064412.

[59] Santanu Pal, Anirban Mukherjee, and Siddhartha Lal. “Topological approach to quantum liquid ground states on geometrically frustrated Heisenberg antiferromagnets”. In: *Journal of Physics: Condensed Matter* 32.16 (Jan. 2020), p. 165805. ISSN: 1361-648X. DOI: 10.1088/1361-648x/ab670f. URL: http://dx.doi.org/10.1088/1361-648X/ab670f.

[60] Juraj Hasik and Philippe Corboz. *Incommensurate order with translationally invariant projected entangled-pair states: Spiral states and quantum spin liquid on the anisotropic triangular lattice*. 2023. DOI: 10.48550/ARXIV.2311.05534. URL: https://arxiv.org/abs/2311.05534.

[61] E. Ressouche et al. "Magnetic Frustration in an Iron-Based Cairo Pentagonal Lattice". In: *Physical Review Letters* 103.26 (Dec. 2009). ISSN: 1079-7114. DOI: 10.1103/physrevlett.103.267204. URL: http://dx.doi.org/10.1103/physrevlett.103.267204.

[62] Artem M. Abakumov et al. "Frustrated Pentagonal Cairo Lattice in the Non-Collinear Antiferromagnet $Bi_4Fe_5O_{13}F$". In: *Physical Review B* 87.2 (Jan. 2013). ISSN: 1550-235X. DOI: 10.1103/physrevb.87.024423. URL: http://dx.doi.org/10.1103/physrevb.87.024423.

[63] I. Rousochatzakis, A. M. Läuchli, and R. Moessner. "Quantum magnetism on the Cairo pentagonal lattice". In: *Physical Review B* 85.10 (Mar. 2012). ISSN: 1550-235X. DOI: 10.1103/physrevb.85.104415. URL: http://dx.doi.org/10.1103/physrevb.85.104415.

[64] Hiroki Nakano, Makoto Isoda, and Tôru Sakai. "Magnetization Process of the $S = 1/2$ Heisenberg Antiferromagnet on the Cairo Pentagon Lattice". In: *Journal of the Physical Society of Japan* 83.5 (May 2014), p. 053702. ISSN: 1347-4073. DOI: 10.7566/jpsj.83.053702. URL: http://dx.doi.org/10.7566/jpsj.83.053702.